remote sensing

MDPI

Article

MT-InSAR and Dam Modeling for the Comprehensive Monitoring of an Earth-Fill Dam: The Case of the Benínar Dam (Almería, Spain)

Miguel Marchamalo-Sacristán [1,*], Antonio Miguel Ruiz-Armenteros [2,3,4], Francisco Lamas-Fernández [5], Beatriz González-Rodrigo [6], Rubén Martínez-Marín [1], José Manuel Delgado-Blasco [4], Matus Bakon [7,8], Milan Lazecky [9,10], Daniele Perissin [11,12], Juraj Papco [13] and Joaquim J. Sousa [14,15]

1 Department of Land Morphology and Engineering, Universidad Politécnica de Madrid, 28040 Madrid, Spain; ruben.martinez@upm.es
2 Department of Cartographic, Geodetic and Photogrammetry Engineering, University of Jaén, Campus Las Lagunillas s/n, 23071 Jaén, Spain; amruiz@ujaen.es
3 Center for Advanced Studies in Earth Sciences, Energy and Environment (CEACTEMA), University of Jaén, Campus Las Lagunillas s/n, 23071 Jaén, Spain
4 Research Group RNM-282 Microgeodesia Jaén, University of Jaén, Campus Las Lagunillas s/n, 23071 Jaén, Spain; jdblasco@ujaen.es
5 Department of Civil Engineering, University of Granada, 18071 Granada, Spain; flamas@ugr.es
6 Department of Environmental and Forestry Management and Engineering, Universidad Politécnica de Madrid, 28040 Madrid, Spain; beatriz.gonzalez.rodrigo@upm.es
7 Insar.sk Ltd., Lesna 35, 080 01 Presov, Slovakia; matus.bakon@insar.sk
8 Department of Finance, Accounting and Mathematical Methods, Faculty of Management and Business, University of Presov, 080 01 Presov, Slovakia
9 School of Earth and Environment, University of Leeds, Leeds LS2 9JT, UK; M.lazecky@leeds.ac.uk
10 IT4Innovations, VSB-TU Ostrava, 708 33 Ostrava-Poruba, Czech Republic
11 Raser Limited, Hong Kong, China; daniele.perissin@sarproz.com
12 CIRGEO, Università degli Studi di Padova, 35020 Padova, Italy
13 Department of Theoretical Geodesy and Geoinformatics, Slovak University of Technology in Bratislava, 810 05 Bratislava, Slovakia; juraj.papco@stuba.sk
14 Department of Engineering, School of Sciences and Technology, Universidade de Trás-os-Montes e Alto Douro, 5000-801 Vila Real, Portugal; jjsousa@utad.pt
15 Institute for Systems and Computer Engineering, Technology and Science INESC-TEC, 4200-465 Porto, Portugal
* Correspondence: miguel.marchamalo@upm.es

Abstract: The Benínar Dam, located in Southeastern Spain, is an earth-fill dam that has experienced filtration issues since its construction in 1985. Despite the installation of various monitoring systems, the data collected are sparse and inadequate for the dam's lifetime. The present research integrates Multi-Temporal Interferometric Synthetic Aperture Radar (MT-InSAR) and dam modeling to validate the monitoring of this dam, opening the way to enhanced integrated monitoring systems. MT-InSAR was proved to be a reliable and continuous monitoring system for dam deformation, surpassing previously installed systems in terms of precision. MT-InSAR allowed the almost-continuous monitoring of this dam since 1992, combining ERS, Envisat, and Sentinel-1A/B data. Line-of-sight (LOS) velocities of settlement in the crest of the dam evolved from maximums of −6 mm/year (1992–2000), −4 mm/year (2002–2010), and −2 mm/year (2015–2021) with median values of −2.6 and −3.0 mm/year in the first periods (ERS and Envisat) and −1.3 mm/year in the Sentinel 1-A/B period. These results are consistent with the maximum admissible modeled deformation from construction, confirming that settlement was more intense in the dam's early stages and decreased over time. MT-InSAR was also used to integrate the monitoring of the dam basin, including critical slopes, quarries, and infrastructures, such as roads, tracks, and spillways. This study allows us to conclude that MT-InSAR and dam modeling are important elements for the integrated monitoring systems of embankment dams. This conclusion supports the complete integration of MT-InSAR and 3D modeling into the monitoring systems of embankment dams, as they are a key complement to traditional geotechnical monitoring and can overcome the main limitations of topographical monitoring.

Citation: Marchamalo-Sacristán, M.; Ruiz-Armenteros, A.M.; Lamas-Fernández, F.; González-Rodrigo, B.; Martínez-Marín, R.; Delgado-Blasco, J.M.; Bakon, M.; Lazecky, M.; Perissin, D.; Papco, J.; et al. MT-InSAR and Dam Modeling for the Comprehensive Monitoring of an Earth-Fill Dam: The Case of the Benínar Dam (Almería, Spain). *Remote Sens.* **2023**, *15*, 2802. https://doi.org/10.3390/rs15112802

Academic Editor: João Catalão Fernandes

Received: 24 March 2023
Revised: 11 May 2023
Accepted: 25 May 2023
Published: 28 May 2023

Keywords: InSAR; embankment dams; FEM; auscultation; subsidence

1. Introduction

Embankment dams are the most common type of dams in the world and collectively represent 78% of all dams; embankment dams can be divided into earth-fill (65%) and rock-fill (13%) dams [1]. They are the oldest type of dams in human history and the most versatile in terms of adapting to different geologies and locations. Accordingly, 80% of dam failures in the world are associated with embankment dams, reflecting their prevalence. A dam failure occurs when part of a dam or its foundation collapses or moves, resulting in the inability to retain water. In most cases, the failure of a dam results in the discharge of substantial volumes of water, which can pose a significant threat to individuals and/or assets situated downstream [2].

The main causes of failure in embankment dams, according to ICOLD [2], are over-topping, internal erosion of the dam body, and movement or leakage of the foundations. A different study conducted on embankment dams built prior to 1986 concluded that almost half of the embankment dam failures (approximately 46%) were caused by piping, with body erosion and foundation erosion accounting for 30.5% and 14.8%, respectively. Furthermore, 36% of the failures resulted from over-topping, 12% were due to spill-gate malfunctions, and 6% were attributed to landslides [3].

Global trends are rapidly changing the needs and requirements of water supply systems around the world, especially in regions where droughts increased in recent decades [4,5]. Adapting dams to ongoing changes is crucial as they play a vital role in supplying water and energy. Dam construction and management is one of the main adaptation strategies used in response to climate change. Given their importance as critical infrastructures, the consequences of a dam's failure can be significant in terms of both economic and social impacts. These infrastructures have associated risks that must be properly managed through a continuous and updated process [6,7]. The rapid changes in factors driving dam risks are likely to make traditional surveillance programs inadequate for long-term dam safety management [8–10].

Satellite radar interferometry (InSAR) uses the radar phase information from SAR images obtained from the same area at different times. With two SAR images, an interferogram can be formed, which is the core of the technique. Differential InSAR (DInSAR) works through comparing two or more radar images of the same location taken at different times and measuring the differences in the radar signals caused by changes in the ground surface. The first DInSAR applications utilized data from the Seasat satellite [11]. For a more comprehensive review of this technique, readers are referred to Bamler and Hartl [12] or Rosen et al. [13], among other studies. InSAR-based techniques are affected by important limitations, including temporal and/or geometric decorrelation, difficulties in phase unwrapping, and errors produced via atmospheric artifacts. To overcome these limitations, several Multi-Temporal (MT-InSAR) techniques were developed in recent years. To extract the deformation phase component, these methods employ stacks of numerous SAR images captured over the same region and utilize advanced data processing and analysis techniques to differentiate various phase components, such as topography and atmosphere. The primary objective of these techniques is to pinpoint areas with minimal noise in the SAR images, which primarily stem from two types of reflectors, namely Persistent Scatterers (PS) and Distributed Scatterers (DS), based on their radar response. Currently, there are two broad types of MT-InSAR techniques: Persistent Scatterers (PSI) methods [14–16] and Small Baseline (SB) methods [17,18], as well as their combinations [19,20].

MT-InSAR is gaining popularity in the field of monitoring ground and infrastructure displacements, particularly in urban areas, as evidenced by Zhu et al., Susaki et al., and García et al. [21–23]. Furthermore, its effectiveness was examined in dam monitoring

during regular operation [24,25] and in high-risk scenarios, such as seismic events [26] and the dam-filling period [27].

This study aims to assess the suitability of integrating MT-InSAR into the monitoring system of the Benínar earth-fill dam located in Almería, Southeastern (SE) Spain. Since its construction, the dam has encountered a distinct issue due to geological filtrations. The situation worsened in August 2004 when a substantial sinkhole collapse occurred near the previously existing Benínar village, resulting in the implementation of a rule that established a maximum water level. This rule drastically reduced the dam's storage capacity [28]. This decision was supported by a previous study that estimated the filtrations at different water levels [29].

Within this study, the original design of the dam is modeled using the Finite Element Method (FEM), considering geological and geotechnical parameters. FEM stability modeling and limit equilibrium methods were carried out to verify the dam's stability in accordance with the measured movements. Through employing MT-InSAR processing on SAR images acquired by the ERS-1/2, Envisat, and Sentinel-1 satellites, the dam's movements from 1992 to 2021, as well as those of the adjacent regions, can be determined. The progression of the dam's subsidence, as predicted through the maximum modeled deformation, is verified through analyzing this series of movements. Additionally, active slope movements are identified through this process.

This study aims to establish the basis for quasi real-time control systems that combine traditional measurements, remote sensing, and modeling approaches to improve monitoring and enable swift responses in earth-fill dams. Integrated systems provide a novel, accurate, and cost-effective method of monitoring the dam body and reservoir basin, which can be utilized as input for safety management plans for hydraulic infrastructures.

2. Characterization of the Benínar Dam

2.1. Study Site

The Benínar Dam is located on the Río Grande de Adra in the municipality of Benínar, in Almería Province, SE Spain (Figure 1). The Río Grande de Adra originates in the Sierra Nevada and receives water from several tributaries. The Benínar Reservoir collects water from a basin of 521 km^2 with an average annual contribution of 45 hm^3. The dam was constructed using local materials with a inclined clay core. Its reservoir, which is located in an area with highly variable rainfall, covers an average area of 235 ha and experiences an annual average of approximately 450 mm of rainfall [30].

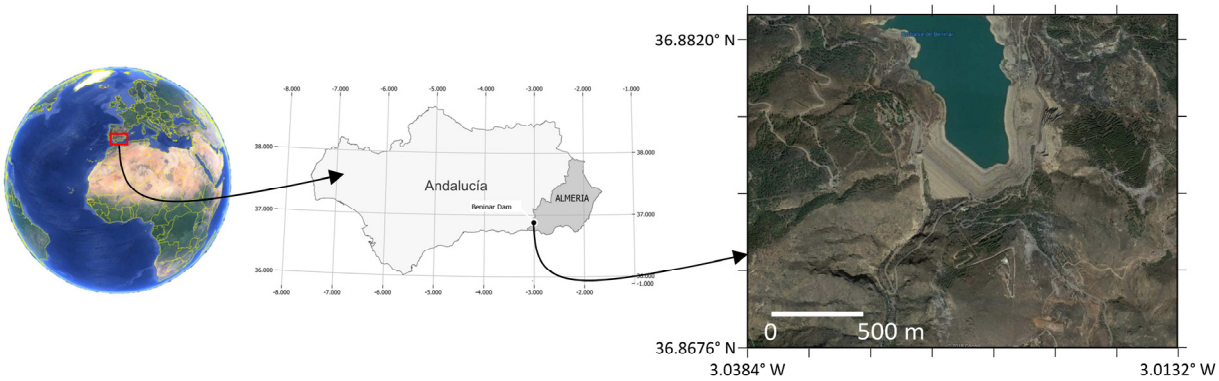

Figure 1. Benínar Reservoir location (Almería, Andalucía, Spain).

The construction of the dam commenced in 1974 and was completed in 1983, although it was not put into service until 1988, following various projects to waterproof the base. However, 32 years after its construction, the dam experienced several leakage problems. The initial design, as well as the complicated and unfavorable geological features, contributed to operational challenges. In early 1991, the authorities reviewed the initial focus of the regulatory project and took actions to capture the reservoir water that was seeping

into the underlying carbonate aquifer [28]. Presently, the dam is employed for irrigation purposes, providing water to the highly productive agriculture region of Campo de Dalías; however, it is not utilized for drink water.

2.2. Geological Framework

Two primary formations make up the reservoir's location: the lower tectonic unit (UTI, Lújar Mantle) and the upper tectonic unit (UTS, Alcázar & Murta Mantles) (Figure 2). Both formations have similar stratigraphy, with an upper level of Upper Triassic carbonate lithologies (limestones and dolomites) based on a Permian–Triassic level of schists and phyllites, which are arranged at the base or interspersed between the carbonaceous-gypsiferous formations [31]. The upper tectonic unit is distributed throughout the central and northern zones of the reservoir, while the lower tectonic unit dominates at the dam site [28].

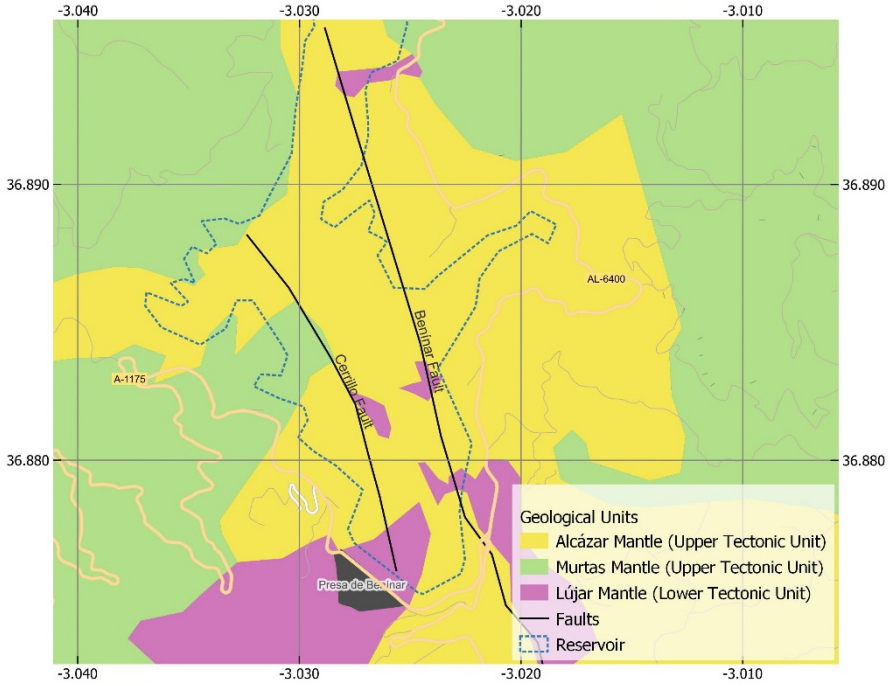

Figure 2. Geological framework of Benínar Dam after [28,29].

These lithologies exhibit a certain entity and continuity in the upper parts, while on the slopes that flow into the reservoir, they appear in the form of blocks fragmented due to gravitational landslides [32]. In the central and northern parts of the reservoir, boreholes cut carbonate lithologies within the UTS, showing phyllites with continuous development. These lithologies can be large slipped limestone blocks (from the upper tectonic units) [33].

The reservoir basin is located on two different groups of materials:

(A) The body of the dam is located on permeable formations (limestone and dolomites from lower UTI). These formations are crossed from NNW to SSE by parallel faults (Benínar and Cerrillo) and associated fractures. These formations were covered in the construction by a more impermeable phyllite layer on which the body of the dam sits directly.

(B) The main reservoir is located on alluvial materials from both mantles and outcrops of the upper UTS (Alcázar & Murta Mantles)

As shown in Figure 2, outcrops of permeable lithologies (limestones and dolomites) appear in the reservoir among alluvial materials. This issue made it necessary to carry out waterproofing works using impervious blankets [34], called "Tapices", designed to cover the outcrops of permeable rocks to limit the filtrations. The treatments included a 3-m-thick layer of phyllites, below a 1-m-deep filter, and a top cover of 1.5-m-thick riprap.

On the other hand, the materials that make up the area of the reservoir present phenomena of historical instability derived from their nature and the high slopes they present, which increased with the operations of the reservoir. The rapid variations in the reservoir load level, which were derived from the reservoir management itself, led to the reactivation of gravitational movements along the reservoir basin and, in particular, the appearance of a landslide that affects the right bank of the reservoir near the front of the dam (dam–village area).

2.3. Structure and Characteristics of the Dam

The Benínar Dam is categorized as a loose material type and has a varied profile, consisting of a phyllite impermeable core. It has a height of 83 m above the river and 87 m above the foundations (as illustrated in Figure 3). The crest length of the dam is 380 m and the width is 11 m. The upstream slope has a ratio of 3.4:1, with a 2:1 ratio from level 360 to the crest. Meanwhile, the downstream slope has a ratio of 1.7:1 and features three 3-m-wide berms situated at levels 307, 327, and 347. Additionally, the dam has a perimeter gallery situated at the point of contact between the core and the phyllites.

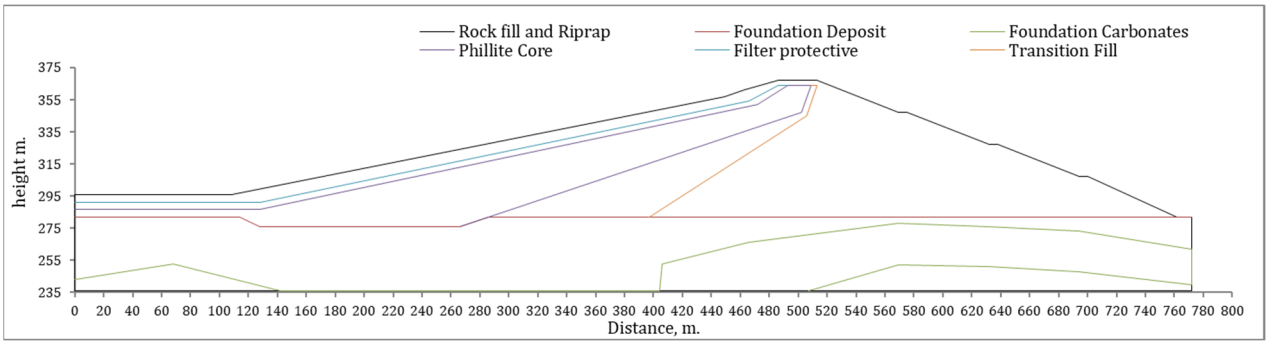

Figure 3. Benínar Dam: profile of study.

The ordinary reservoir's maximum height is 360 m, while the extraordinary reservoir reaches a maximum height of 363.50 m, even though the maximum permissible height has been 328 m since 2004. The dam's crest is situated at an elevation of 367 m. The total volume of the reservoir is 68.12 hm^3. The spillway, which is located on the right bank, comprises three 6-m-wide spans divided by two 3-m-wide piers and has three 4-m-high gates, with a maximum capacity of 500 m^3/s. On the left bank, there is an intermediate intake for supply and irrigation, with a maximum drainage capacity of 38.9 m^3/s. The right bank of the dam is home to a small village and the maintenance and operation facilities of the reservoir.

An exceptional characteristic of the dam is its inclined core that tilts in the upstream direction, connecting the dam's waterproofing element to the waterproof material outcrops of the abutments and upstream. This characteristic grants the dam a watertight structure, removing the necessity for costly waterproof injections into the permeable foundation.

2.4. Geotechnical Parameters of the Dam Materials

According to the geometric characteristics of the dam and in accordance with Article 3.1 of the Technical Regulation for Safety of Dams and Reservoirs [35], the dam is classified as a large dam and falls under Category A. The geotechnical characteristics of the different materials used in the reservoir basin were studied and characterized (Table 1).

The impervious core of the dam was constructed using outcropping phyllites ("launas") found in close proximity to the dam. The formation contains intercalations of quartzites that needed to be removed from the original material before being placed in the dam. The material used for the core was obtained from a quarry, where it was determined that the phyllites contained less than 1.4% sulphates, had a permeability of 10^{-7} m/s, and had an internal friction angle ranging from 25° to 30°.

Table 1. Geotechnical properties of materials used in construction of Benínar Dam.

Material	E (t/m^2)	ν	γ (t/m^3)	c (t/m^2)	ϕ° Deg.	k_1 (m/s)	k_2 (m/s)	k_2/k_1	W_{nat}	T_{max} cm	% < 0.08 mm
Rockfill	20,000	0.3	2.2	2.5	45	0.1	0.1	1	1.5	67.0	1.8
Phyllites core	30,000	0.3	2.1	8	25	10^{-7}	10^{-7}	1	20	4.5	89.4
Fine filter	8000	0.3	2.1	1	36	0.01	0.01	1	3.2	2.0	5
River deposit compacted	18,000	0.3	2.0	2.5	33	10^{-4}	10^{-4}	1	12	10	15
River deposit foundation	10,000	0.35	1.9	2	33	10^{-4}	10^{-4}	1			
Limestone foundation	200,000	0.2	2.4	72	24	4×10^{-5}	4×10^{-5}	1			

Note-. E: Young's Module; ν: Poisson's Ratio; γ: Dry density; c: Cohesion; ϕ°: Friction Angle; k_1, k_2: Permeability; W_{ant}: Humidity; T_{max}: Size; % < 0.08: % Fines less than 0.08 mm.

The material used for the dam breakwater was extracted from a nearby quarry (located on the left bank next to the abutment—about 500 m away—and above the reservoir level) that contained fragments of outcropping dolomites and limestone. These materials were considered suitable for forming the breakwater area of the dam, as they provided a thick breakwater with a favourable friction angle and sufficient drainage capacity.

Finally, to complete the calculation profile of the model, the following geotechnical parameters were used for the different areas of the dam and the foundation strata. Six units are defined based on the geological profile of the terrain at the site, and their parameters are presented in Table 1.

3. Materials and Methods

3.1. Modeling the Original Design of Benínar Dam

The stability of the dam body was analyzed via limit the equilibrium method [36–38]. Various methods, including Bishop, Morgenstern–Price, Jambu, and Spencer, were tested using the Rocscience Slide version 6.2 software (Rocscience, Toronto, ON, Canada). Two models were developed: one in steady state and the other at maximum reservoir level. The latter model was studied for a rapid drawdown and in stages. For seismic calculations, the standards set by the Spanish Committee of Large Dams [39] were followed. The project earthquake was defined according to the dam project, which was coherent with the Seismic Resistant Regulations NCSE-O2 [40]. Additionally, the total deformation that would occur at the crest elevation from the beginning of construction to the present day at full reservoir capacity was modeled. For this purpose, the Rocscience Phase2 ver 8.2 software (Rocscience, Toronto, ON, Canada) was used to create two models with the same characteristics, as described in the stability calculation.

With regards to the full reservoir scenario, it was assumed that both the central and lateral portions of the nucleus possessed equivalent permeability. While this assumption may not reflect the reality, it was a conservative estimate. Furthermore, various degrees of rapid drawdown were examined at different water levels (2/3, 1/2, and 1/3 of the reservoir's height).

Typically, the minimum safety factor for slope stability during discharge did not support the assumption of complete emptying of the reservoir [41]. Instead, an intermediate outlet between one-third and one-half of the height was usually considered.

The study was conducted on a geological cross-sectional profile, considering the terrain's and the tectonic and hydrogeological conditions of the boundary. The definition of this profile was based on the available comprehensive geological and geophysical study [28]. One noteworthy input of this study was the map displaying isolines of the river sediment package. The map played a crucial role in comprehending the shape of the boundary

between the alluvial layer and the geological foundation. With the aid of these data, the most relevant geological cross section for the stability analysis was created.

Displacement magnitudes were modeled along the dam axis and the shoulders of the structure, along with the traction forces that could be generated with minimum safety factors and the maximum potential deformations at the critical safety factor. These analyses were conducted to assess the stability of the dam body. To this end, scenarios involving maximum reservoir capacity and rapid discharge were considered, both at zero level and at 334.5 m. Furthermore, given the seismic risk associated with the area, we examined the responses to high-intensity seismic activity that was not tectonic in nature.

3.2. Auscultation System at the Benínar Dam

During and after the construction, various monitoring systems were implemented at the Benínar Dam, including 13 vibrating wire piezometers, 54 hydraulic piezometers, 74 hydraulic pressure cells, 3 subsidence tubes, 3 accelerographs, and 8 and 2 topographic benchmarks. However, a detailed follow-up report in 2012 [28] indicated that most of these devices were no longer functioning. Therefore, for the scope of this paper, only the topographic series between 2015 and 2018 is accessible.

In 1985, eight topographic targets were installed at Benínar Dam to monitor deformations using collimation from two external bases; however, no measurement records are available from 1985 to 2015. From 2002 to 2015, no topographic measurements were taken at the dam. In 2015, a topographical network was established, consisting of 29 permanent targets embedded in the dam, which were measured regularly using a total station, recording X, Y, and Z over time. In compliance with the safety plan for the Benínar Dam, six measurement campaigns were conducted from September 2015 to June 2016, followed by a gap in data collection between June 2016 and June 2017; subsequently, an additional seven campaigns were conducted from June 2017 to August 2018.

Using traditional topographic methods with a total station, the X, Y, and Z coordinates of the target points (control points) were calculated for each measurement campaign. The changes in coordinates were analyzed as displacements in the three directions. For each target, the differences in X, Y, and Z coordinates from the original date (October 2015) were provided, along with the estimated error for each target. According to the auscultation reports, the error was estimated as the probable error, which was calculated as two-thirds of the maximum error, with the latter being 2.5 times the quadratic mean error. The estimated error ranged from 4 to 20 mm for the Z estimates, considering the characteristics of the total stations used for the monitoring, including a 5^{cc} angular reading error, a 2 mm and 2 ppm distanciometer, and a 5 mm position error [42].

3.3. MT-InSAR Processing

3.3.1. Datasets

In this work, C-band images obtained from European Space Agency (ESA) satellites, specifically ERS-1/2, Envisat, and Sentinel-1A/B, were processed over a period of 30 years spanning from 1992 to 2022. In particular, we used 22 SLC ERS-1/2 SAR descending images, which were acquired between 6 June 1992 and 31 October 2000; 32 SLC Envisat ASAR ascending images, which were obtained between 3 December 2002 and 29 June 2010; 360 SLC IW Sentinel-1A/B ascending images, which were collected from 10 March 2015 to 27 December 2021; and 352 SLC IW Sentinel-1A/B descending images, which were gathered from 16 March 2015 to 21 December 2021 (Table 2).

The ERS-1/2 images were acquired with a look angle of 23° and a nominal spatial resolution of 5 × 25 m (azimuth × range). Similarly, the Envisat images were captured with a look angle of 23° in the middle swath IS2 and a nominal pixel dimension of 5 × 25 m (azimuth × range). In contrast, the Sentinel-1A/B images had a look angle of approximately 39° in the ascending geometry of Track 1 subswath 2, while the descending Sentinel-1A/B images had a look angle of approximately 34° (Track 81). Both Sentinel-1A/B ascending and descending images had a pixel spacing of 2.3 × 14.1 m (range × azimuth).

Table 2. Summary of SAR datasets used in this study, covering a time period of about 30 years.

Satellite/s	Temporal Span	Revisiting Time (Days)	Number of Images	Orbit Direction	Acquisition Looking Direction	Look Angle [°]	Azimuth Heading Angle [°]
ERS 1/2	06/1992–10/2000	35	22	Desc	West	23	198.1
Envisat	12/2002–06/2010	35	32	Asc	East	23	347.0
Sentinel-1 A/B	03/2015–12/2021	6/12	360	Asc (T1)	East	39.21	349.9
Sentinel-1 A/B	03/2015–12/2021	6/12	360	Desc (T81)	West	34.03	190.7

3.3.2. MT-InSAR Methodology

Satellite Multi-temporal Interferometry (MT-InSAR) is an advanced multi-temporal satellite radar interferometry technique used for monitoring ground deformation. MT-InSAR aims to identify radar targets with high phase stability over time, which can be used as a natural point network for monitoring terrain motion. Through analyzing the interferometric phase of these targets, displacement maps with millimeter precision can be generated over wide areas via utilizing frequent satellite acquisitions. The fundamental concepts underlying the multi-temporal InSAR approaches used in this work are summarized. For a detailed description, it is recommended to refer to [14,16,43,44].

Among MT-InSAR techniques, we used the classical PSI. Its main objective is to estimate the relative height and displacement of persistent ground scatterers through the analysis of stable electromagnetic signatures in the interferometric phase, i.e., temporal phase differences (Equation (1)).

$$\Delta\phi = \Delta\phi^{flat} + \Delta\phi^{height} + \Delta\phi^{disp} + \Delta\phi^{atmo} + \Delta\eta \quad (1)$$

The interferometric phase was composed of the following contributions: flat earth, $\Delta\phi^{flat}$; topography/height, $\Delta\phi^{height}$; displacement/deformation, $\Delta\phi^{disp}$; atmospheric delay, $\Delta\phi^{atmo}$; and noise, $\Delta\eta$. Phase contributions are were estimated, to extract the displacement or deformation that corresponds to the observed phase differences. The contribution of displacement to the phase, $\Delta\phi^{disp}$, was linear with the baseline perpendicular to the radar line of sight, B_n, and with the potential movement of the target, Δv (Equation (2)):

$$\Delta\phi^{disp} = \frac{4\pi}{\lambda}\Delta v.B_t \quad (2)$$

The most common approach to modeling displacement is to assume that it has a temporal dependence that can be considered linear. However, this assumption is not always accurate, and it is crucial to detect cumulative or non-linear displacement [45]. In conclusion, this technique can be seen as a set of equations, where the unknowns are the height (Δh) and velocity (Δv) between individual points, forming a network of estimates. One solution to solve the system comes from maximizing the periodogram in which height and velocity represent the two-dimensional frequencies to be estimated. The mathematical formula for the periodogram, $\xi[\Delta v, \Delta h]$ [14,43] is given by Equation (3).

$$\xi[\Delta v, \Delta h] = \frac{1}{N}\sum e^{j[\Delta\phi - \Delta\phi^{disp} - \Delta\phi^{height}]} \quad (3)$$

The solution is given using the pair, $\Delta\widetilde{v}, \Delta\widetilde{h}$o, which maximize the absolute value of the periodogram (Equation (4)).

$$\Delta\widetilde{v}, \Delta\widetilde{h} = argmax\{|\xi[\Delta v, \Delta h]|\} \quad (4)$$

The maximum of the absolute value of the periodogram is referred to as temporal coherence (Equation (5)).

$$\widetilde{\xi} = \left| \xi \left[\Delta\widetilde{v}, \Delta\widetilde{h} \right] \right| \quad (5)$$

PS (Persistent Scatterers) are points characterized by their high phase stability and hight temporal coherence. When the model represented by $(\Delta\widetilde{v}, \Delta\widetilde{h})$ corresponded to the observed interferometric phase, the argument of the periodogram in Equation 3 was close to zero, and the temporal coherence tended to 1. Conversely, if the model did not match the observed phase, the argument of the periodogram would be random, and the temporal coherence would have low values. Results from points with low temporal coherence were not reliable, as the model we used to process the InSAR time series did not fit the actual observations. Low values of temporal coherence (e.g., below 0.6) are typically associated with limitations and constraints of InSAR technology [14,16,43,44]. However, in some cases, these low temporal coherences can also represent areas where deformation processes are rapidly progressing in an unexpected or unmodeled manner.

For ERS-1/2 and Envisat datasets, we also used another MT-InSAR technique via the SBAS algorithm [19]. It utilizes all possible combinations of SAR images with small temporal and spatial baselines, and is widely used to reduce spatial decorrelation and residual phase effects caused by uncompensated topography.

3.3.3. Software

The ERS-1/2 and Envisat datasets were processed using a combination of two MT-InSAR methods (PSI and SBAS) implemented with StaMPS-MTI software [19,20,46] a package developed in collaboration by Stanford University (Stanford, CA, USA), University of Iceland (Reykjavík, IS), Delft University (Delft, NL), and University of Leeds (Leeds, GB). Figure 4 shows the distribution of temporal vs. perpendicular baselines for each dataset. Figure 4a,b display the image connections for each method, which are represented in red for PSI and in green for SBAS combinations. Sentinel-1A/B data were analyzed using the standard PSI technique (Figure 4c,d) and implemented via SARPROZ software [47,48].

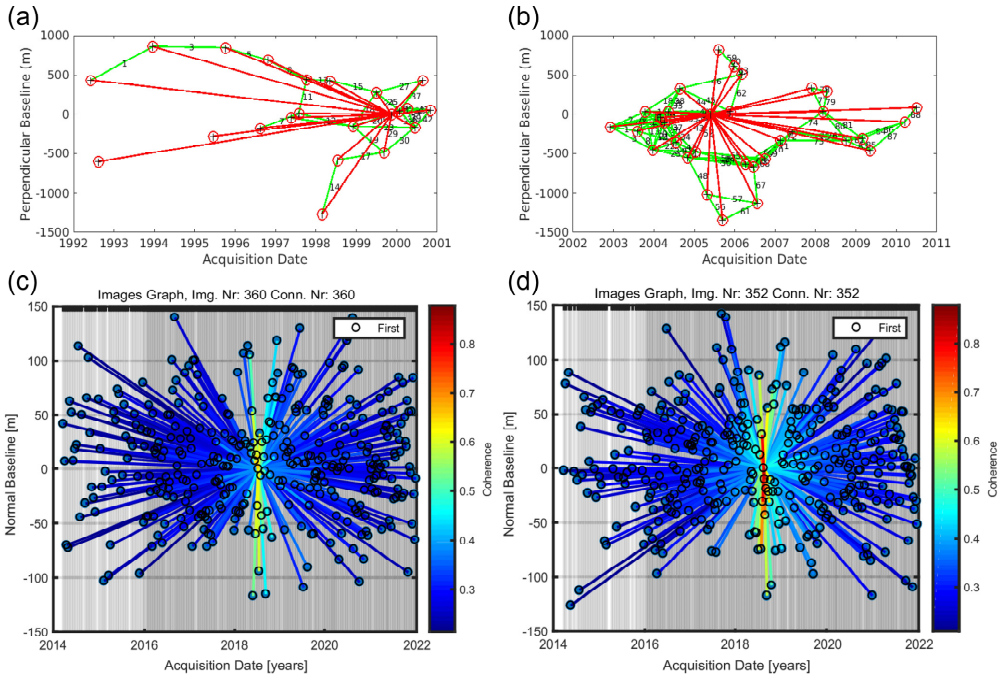

Figure 4. Perpendicular vs. Temporal baselines distributions. Top: (**a**) ERS-1/2 and (**b**) Envisat. Bottom: Sentinel-1A/B (**c**) ascending and (**d**) descending.

The identification of pixels for time-series analysis was based on single-look interferograms that exhibit coherence in time. One of the advantages of the StaMPS-MTI method was its capability to perform 3D phase unwrapping in both spatial and temporal domains, allowing for retrieval of absolute phase values for each pixel. With StaMPS-MTI, the final selection of measuring points obtained with PSI and SBAS could be merged to obtain the final processing output [19] (Figure 5).

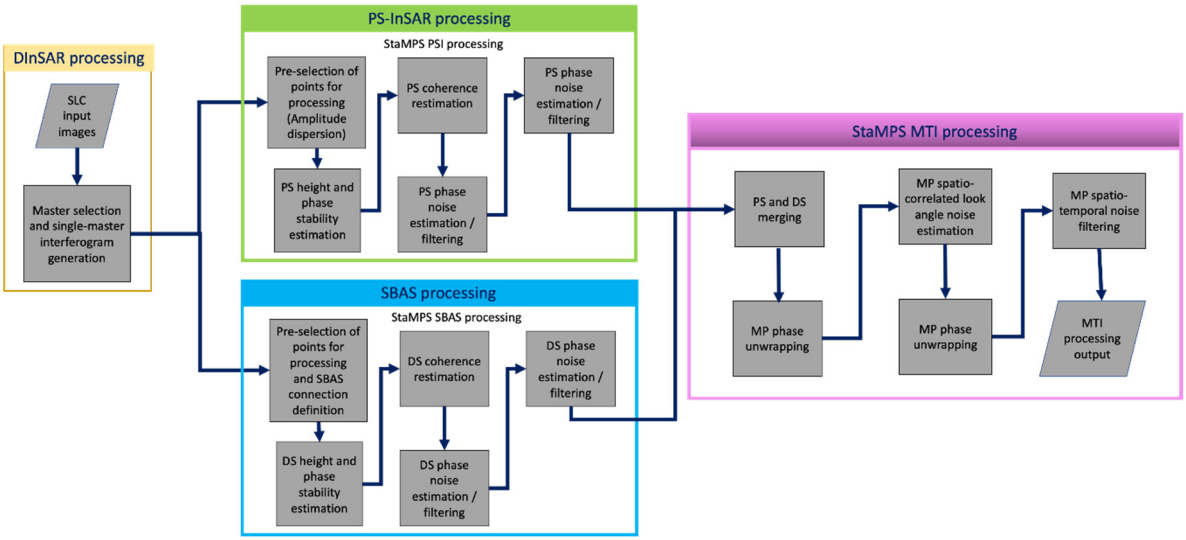

Figure 5. StaMPS-MTI workflow.

For SARPROZ processing, all available SLC images were co-registered on a unique master acquisition. The data were then analyzed on a pixel-by-pixel basis to identify a sparse grid of points, usually corresponding to man-made structures (e.g., buildings, bridges, monuments, antennas, poles, conducts, etc.) or terrain features with high reflectivity. These points were identified to filter out atmospheric noise and compensate for topographic artifacts. Precise Orbit Ephemerides (AUX_POEORB) [49] and a digital elevation model were used for removal of the topographic phase component. To identify precise geolocation of PS points, a single Ground Control Point (GCP) was selected from both sensing geometries (ascending/descending). A combination of quality parameters related to the amplitude of the radar signal was used to pre-select points with stable electromagnetic signature, while a threshold on Amplitude Stability Index [50] was used to create this network of pre-selected points with stable electromagnetic signature. A linear model assumption was used for estimating residual height and displacement velocity, and displacement time-series were estimated for each persistent scattering point with respect to the local reference point (Figure 6).

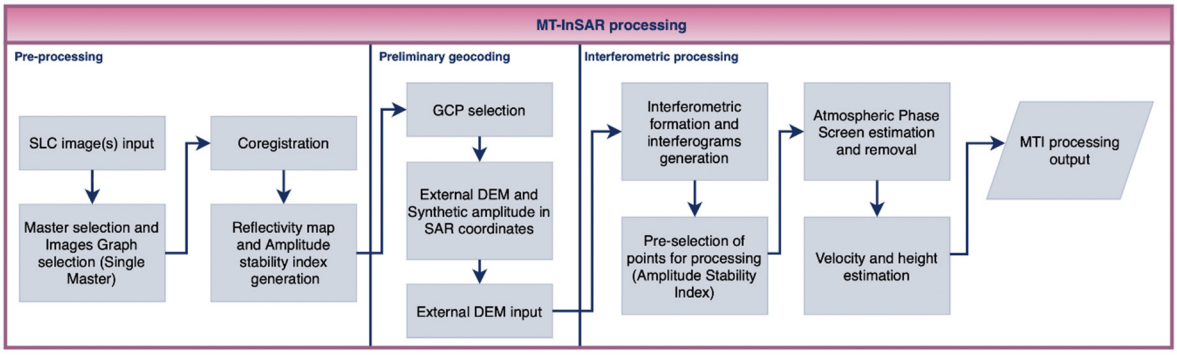

Figure 6. SARPROZ workflow.

The Sentinel-1A/B ascending and descending data were acquired over the same time period, enabling the computation of the decomposition of movements in the vertical and E–W (East–West) directions using the conventional approach [48]. For that process, the first step involved the computation of possible shifts between the ascending/descending datasets through estimating the offsets in longitude, latitude, and height. To obtain precise offsets, points with distances closer than the range specified as a maximum planar distance and with height differences closer than the maximum height distance were used. The ascending/descending pairs were then processed using the same maximum planar and maximum height distances to identify the corresponding points in the two datasets. Once the offsets were estimated and the ascending/descending pairs identified (in the case of ascending and descending dataset pairs), the decomposed movement could be computed using Equations (6) and (7), plotted, and exported. Various options were available for this, such as generating all points, ascending/descending pairs, or a grid created on overlapping areas.

$$\begin{bmatrix} d_{Asc} \\ d_{Desc} \end{bmatrix} = \begin{bmatrix} \sin\theta_{Asc}\cos\varnothing_{Asc} & \cos\theta_{Asc} \\ \sin\theta_{Desc}\cos\varnothing_{Desc} & \cos\theta_{Desc} \end{bmatrix} \cdot \begin{bmatrix} d_{East} \\ d_{Up} \end{bmatrix} = M \begin{bmatrix} d_{East} \\ d_{Up} \end{bmatrix} \quad (6)$$

$$\begin{bmatrix} d_{East} \\ d_{Up} \end{bmatrix} = M^{-1} \cdot \begin{bmatrix} d_{Asc} \\ d_{Desc} \end{bmatrix} \quad (7)$$

where d_{Asc} and d_{Desc} are the mean displacements in the line-of-sight (LOS) direction for the ascending and descending datasets, θ_{Asc} and θ_{Desc} are the looking angles for the ascending and descending LOS directions, $\varnothing_{Asc}$ and $\varnothing_{Desc}$ are the horizontal angles of the LOS directions measured from the east in a clockwise direction, and d_{East} and d_{Up} are the decomposed mean deformations in the east and vertical directions.

For the final analysis, two types of outputs were employed for the studied period: the rates of displacement or velocities (in mm/year) and the time series of displacements (mm). When only one geometry was available (ERS-1/2 and Envisat), the results were presented in LOS direction (for either ascending or descending geometries alone). When decomposition was possible, we presented vertical and East–West components.

4. Results

4.1. Modeling the Design of Benínar Dam

Through employing the aforementioned methodologies, stability, filtration, and deformation analyses were carried out at maximum reservoir capacity and during a sudden drawdown at ground level, as well as at ground level (334.5 m). The outcomes of the analyses are provided in this section.

Figure 7 depicts the distribution of displacements and their vectors at the end of the construction, i.e., the maximum vertical modeled deformation of 19.25 cm in the crest axis. As expected, the section with the greatest movements is situated closest to the upstream slope, where the hydraulic load adds to the progressive increase in the height over foundations. It is also observed that the apex of the elevated block in the fault contributes to a certain reorientation of the movements, causing the isolines to advance towards the upper apex of the core of compacted coatings instead of towards the foundation, owing to the noticeable decrease in the thickness of the compressible sediments downstream of the fault. Critical stability results are expressed in the Safety Reduction Factor (SFR) for all cases. Figure 7 displays the zone of the failure joint that produces a clearly different stress in the transition zone (compacted carries).

The behavioral models reveal that when volumetric deformation occurs (as depicted in Figure 8), the breakwater strips and impermeable core undergo tension when they come into contact with the filter. This tension can cause failure without causing breakage or unstable deformation. Figure 8 illustrates how the deformed mass and displacement vary based on the critical slip circle SRF. The figure clearly shows the fault zone and downstream sectors that are susceptible to admissible deformation.

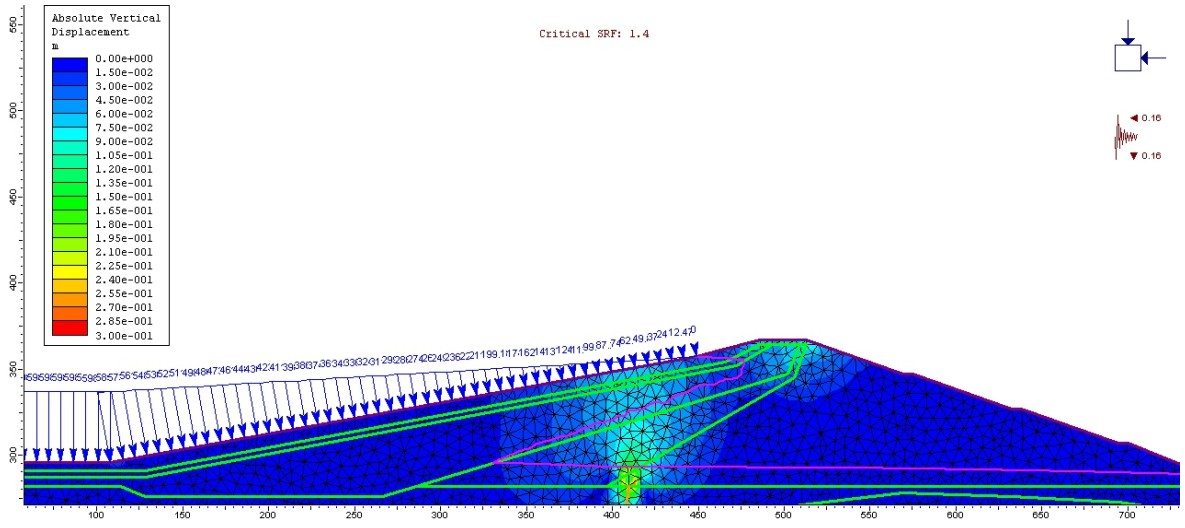

Figure 7. Vertical displacement at full reservoir scenario.

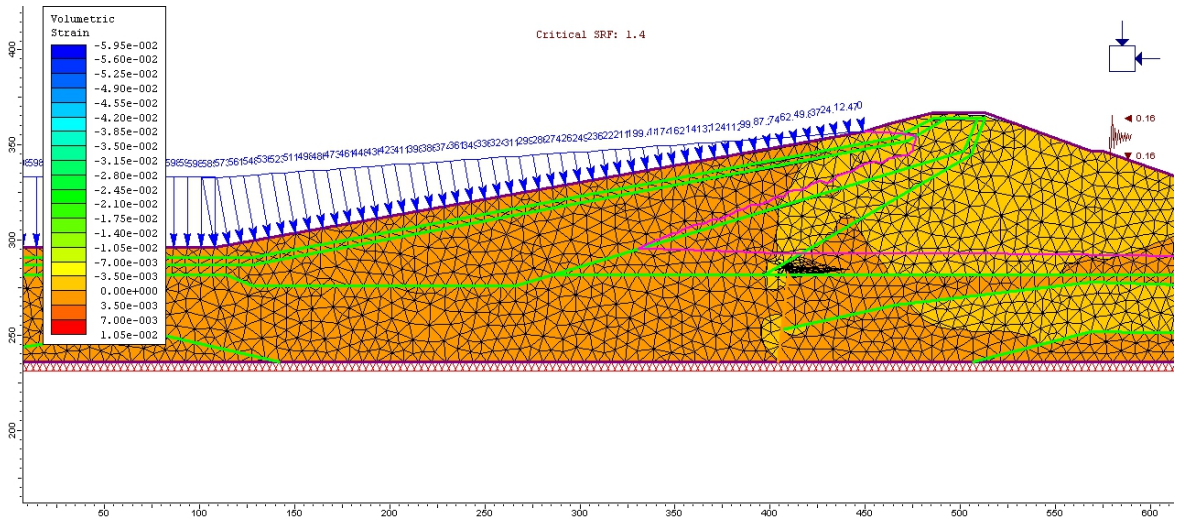

Figure 8. Maximum volumetric deformation zone at full reservoir scenario.

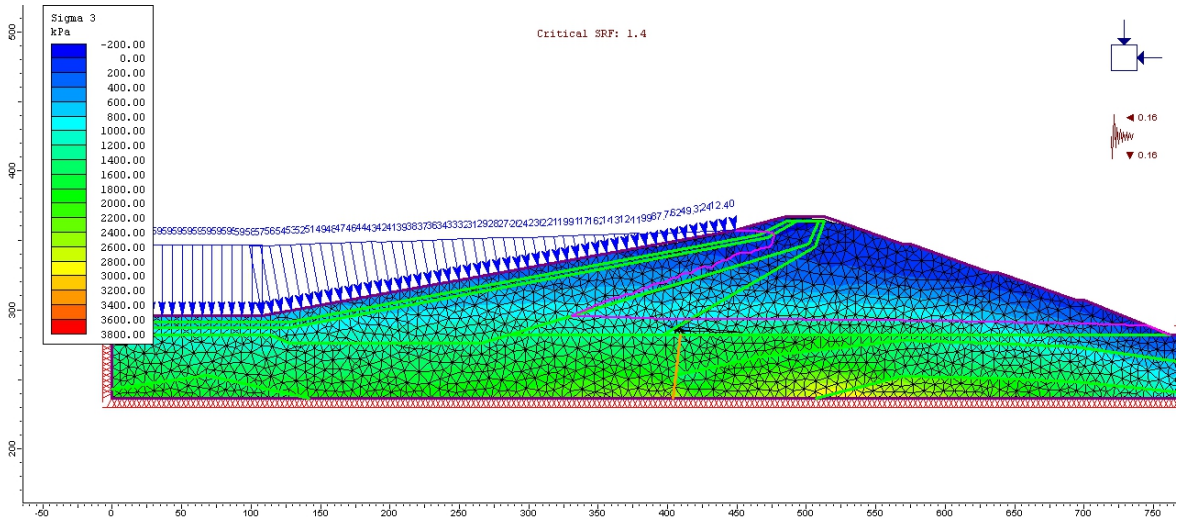

Figure 9. Stress distribution at full reservoir scenario.

Upon analyzing the stress distribution in Figure 9, it can be observed, as evidenced by the representation of the resistance factor, that tensions appear in the aforementioned strips, potentially affecting the phyllites' nuclei in contact with the filter and the rock fill shoulder. The isoline of null values is also visible, and the magnitudes of the detected tensions do not exceed 1.2 Kp/cm^2.

The pore pressure distribution in the filter, core, and transition contact areas (Figure 10) remains uniform with respect to the head pressure. The overall behavior is sufficient for stability, with no issues observed in the fault area.

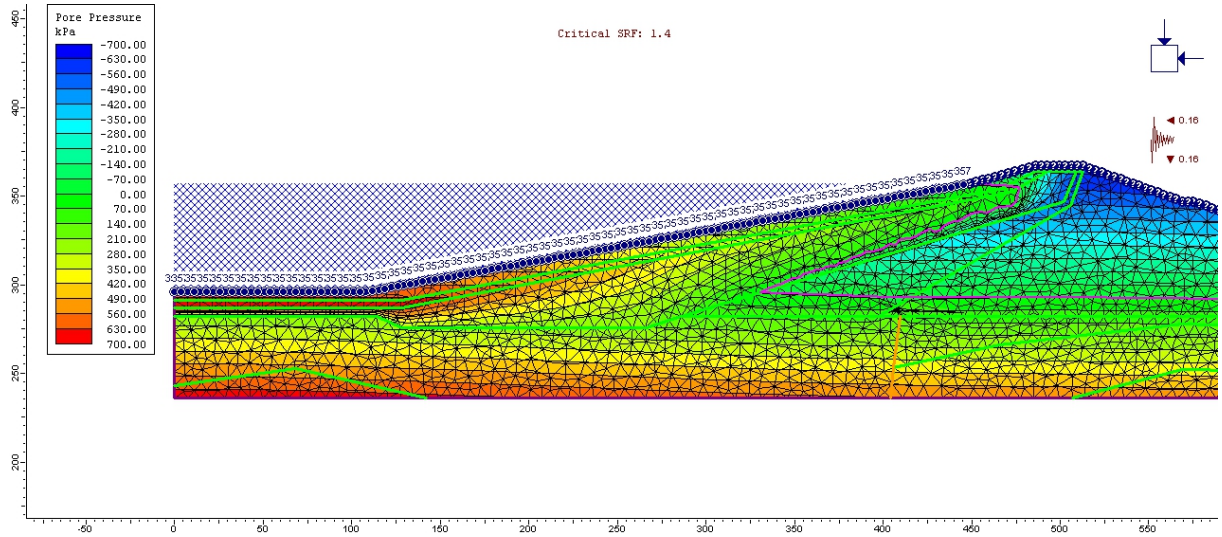

Figure 10. Variation in pore pressure at full reservoir scenario.

When comparing the distribution of total pressures in the full reservoir scenario (Figure 11), the highest stresses occur in the upstream suction zone, as expected.

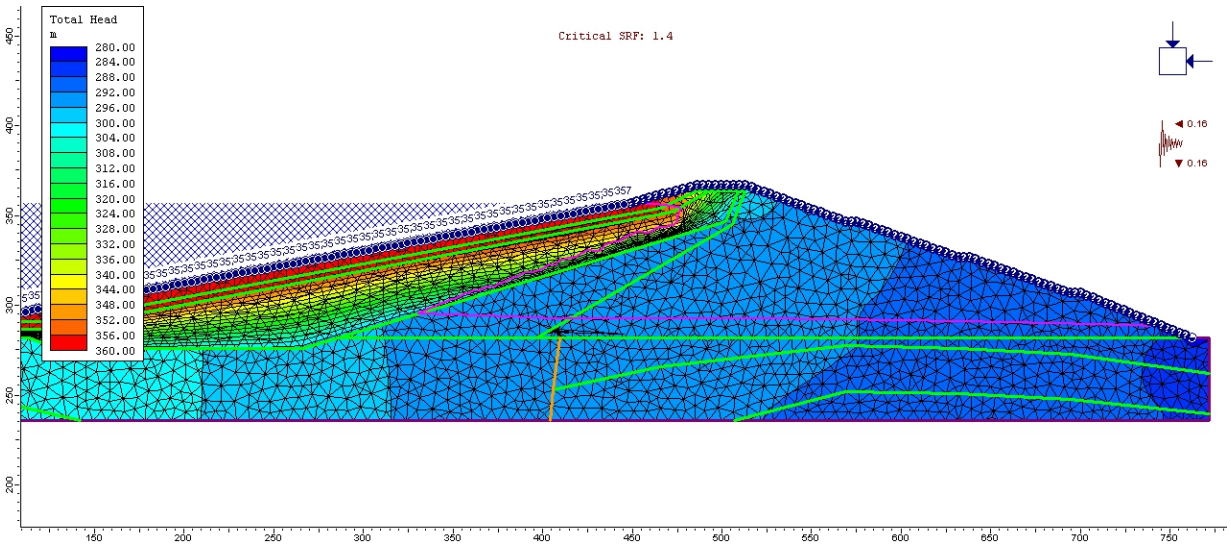

Figure 11. Distribution of total head at full reservoir scenario.

With respect to the limit equilibrium results for the minimum slip circle, the values indicate that the stability conditions are met for all hypotheses analyzed in accordance with the requirements of the Spanish Large Dam Committee [51]. The hypothesis with the lowest values corresponds to total rapid drawdown. The minimum circle safety factors for maximum reservoir are always greater than 2.07. For rapid drawdown at level 334.5, the

factor is 1.86, and for total rapid drawdown, it is always greater than 1.62. Consequently, the dam is stable in all scenarios.

4.2. Dam Deformation Analysis with MT-InSAR

During the first years following its construction (1985–1992), no SAR data were available. The first set of data, which was acquired by the ERS radar sensor, contains values from 6 June 1992 and covers the period up to November 2000. Multi-temporal analysis of this series reveals that the consolidation of the dam was still ongoing, with subsidence in LOS direction at a rate of −5 to −6 mm/year in the upper crest of the dam. During the subsequent radar monitoring period, Envisat ASAR images were processed for the timeframe of 3 December 2002–29 June 2010. It was observed that the consolidation was less active during this period, with LOS subsidence values ranging between −3 and −4 mm/year at the top of the crest. The ascending geometry resulted in more measurement points being available on the upstream slope of the dam and fewer measurements points being available on the downstream slope (Figure 12).

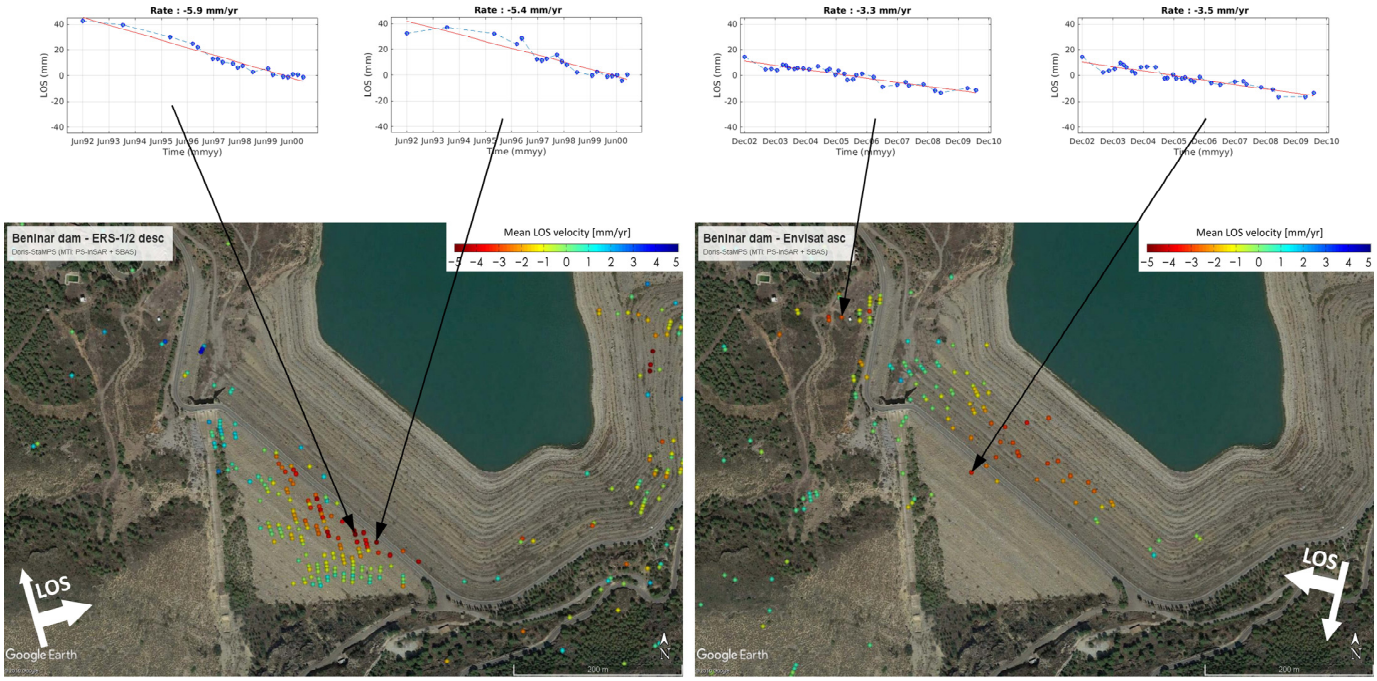

Figure 12. Mean LOS velocity (mm/year) of Benínar Dam calculated from (**left**) 22 ERS-1/2 descending images from period 6 June 1992–31 October 2000 and (**right**) 32 Envisat ascending images from period 3 December 2002–29 June 2010.

The period spanning from 2015 to 2021 displays fewer deformations, confirming the stabilization of the dam settlement post-construction (Figure 13).

The deformation progression of the dam was computed for the central top crest of the structure during the three InSAR monitoring periods (Figure 14). The area of interest was defined as the dam body above 347 m above sea level (first berm), which was centered with a width of 140 m. It is noteworthy that the deformation velocities gradually decreased over time, with median values of −2.6 and −3.0 mm/year in the first periods (ERS and Envisat) falling to −1.3 mm/year in the Sentinel-1A/B period. During this period, vertical and eastward movements were separately analyzed, revealing that the vertical component was dominant, with almost no displacement observed in the East–West direction (Figure 14).

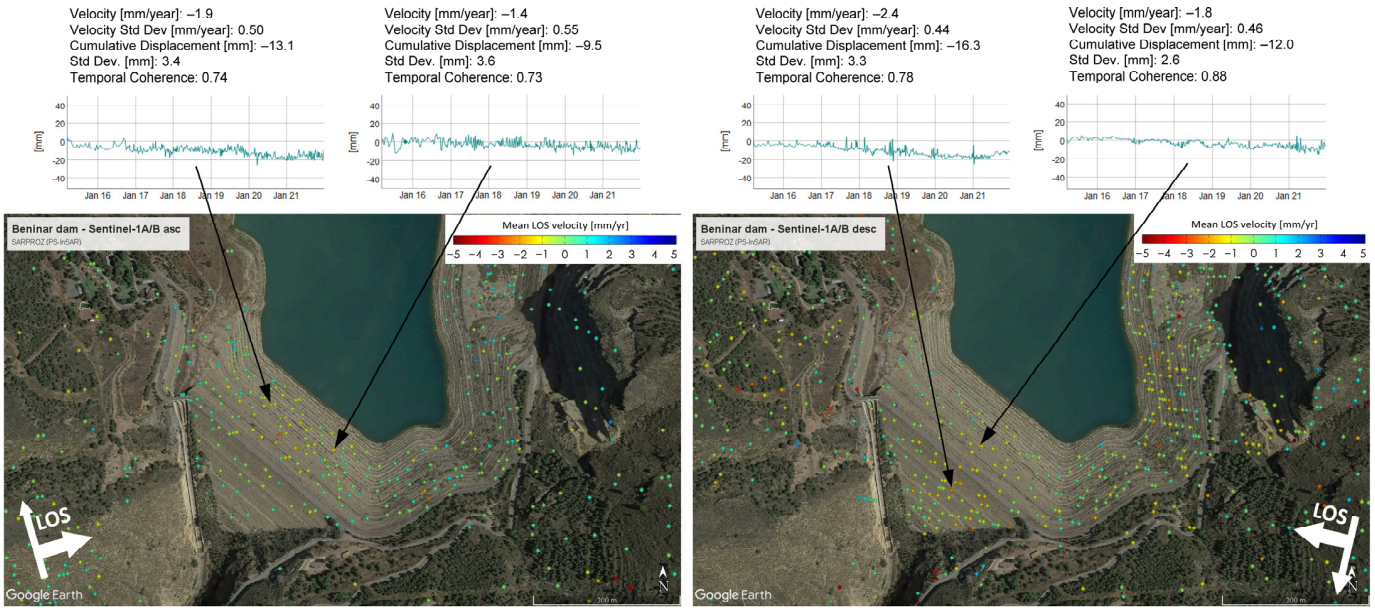

Figure 13. Mean LOS velocity (mm/year) of Benínar Dam computed from ascending (**left**) and descending (**right**) Sentinel-1A/B images in periods 10 March 2015–27 December 2021 (ascending) and 16 March 2015–21 December 2021 (descending).

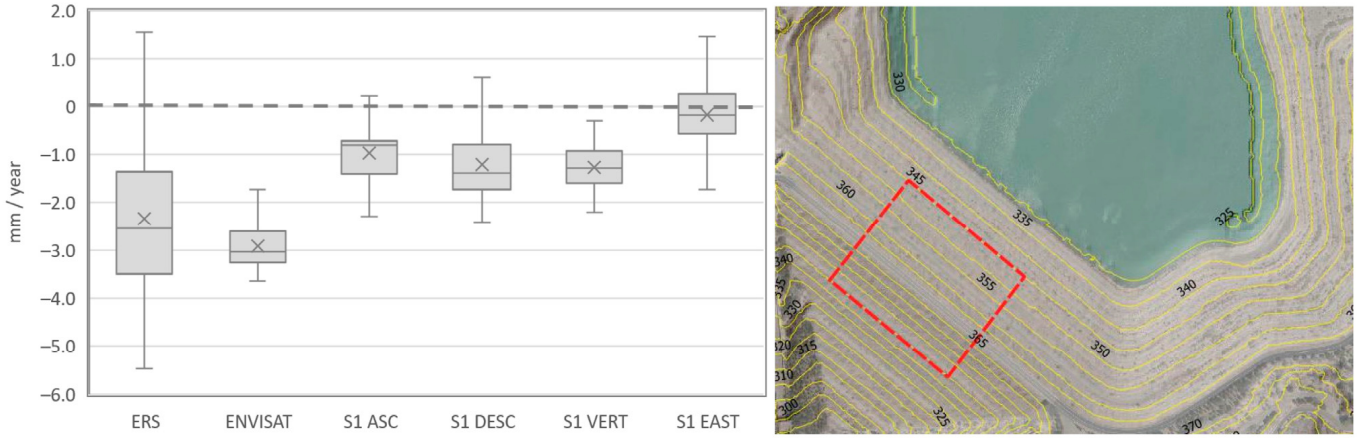

Figure 14. Evolution of dam deformation velocity (in mm/year) along three InSAR monitoring periods (ERS-1992–2000, Envisat 2002–2010, and Sentinel-1A/B 2015–2021) for the central upper part of the dam (red box). All velocities data are presented in LOS direction, except for vertical component (positive upwards) and East–West velocity derived from Sentinel-1A/B (positive to East).

A "cross-section" analysis of the dam deformations in the Sentinel-1 period (2015–2021) is shown in Figure 15. It can be noted that the area including the top crest of the dam (coronation at 367 m) presents the largest deformations, decreasing from up to down both in the downslope direction and in the upstream slope. The deformations are similar at the same heights at both sides of the crest (upstream and downstream), showing more dispersion in the upstream slope.

Figure 16 shows a detailed analysis of the deformation along the berms and the crest of the dam. The analysis confirms that the deformation is greatest in the central part of the dam, as expected.

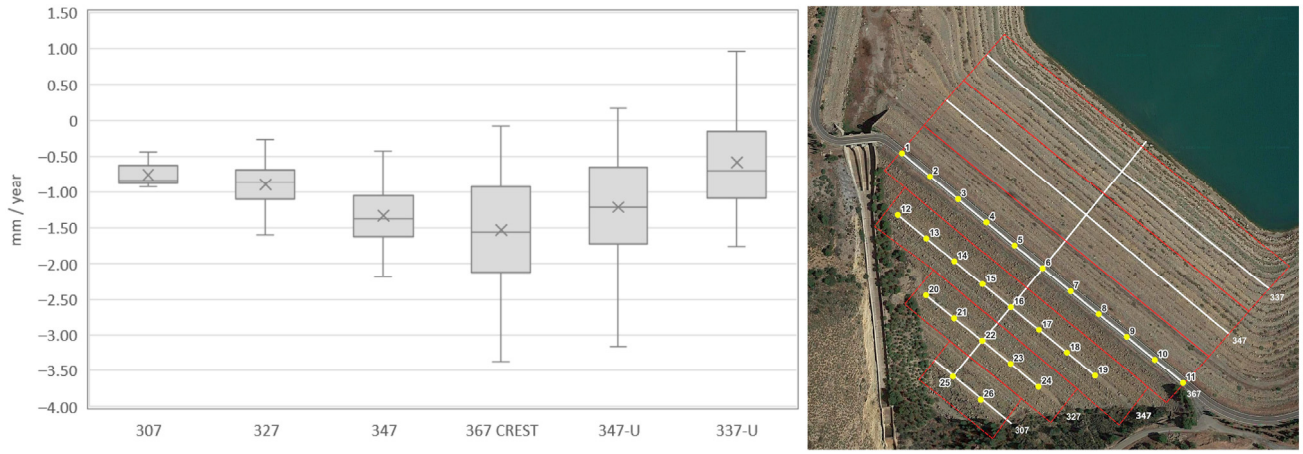

Figure 15. Evolution of dam vertical velocity (in mm/year) in Sentinel-1A/B period (2015–2021) along transversal axis of dam computed for rectangles centered in berms downstream (307, 327, 347), crest of dam (367) and two areas upstream (347U and 337U).

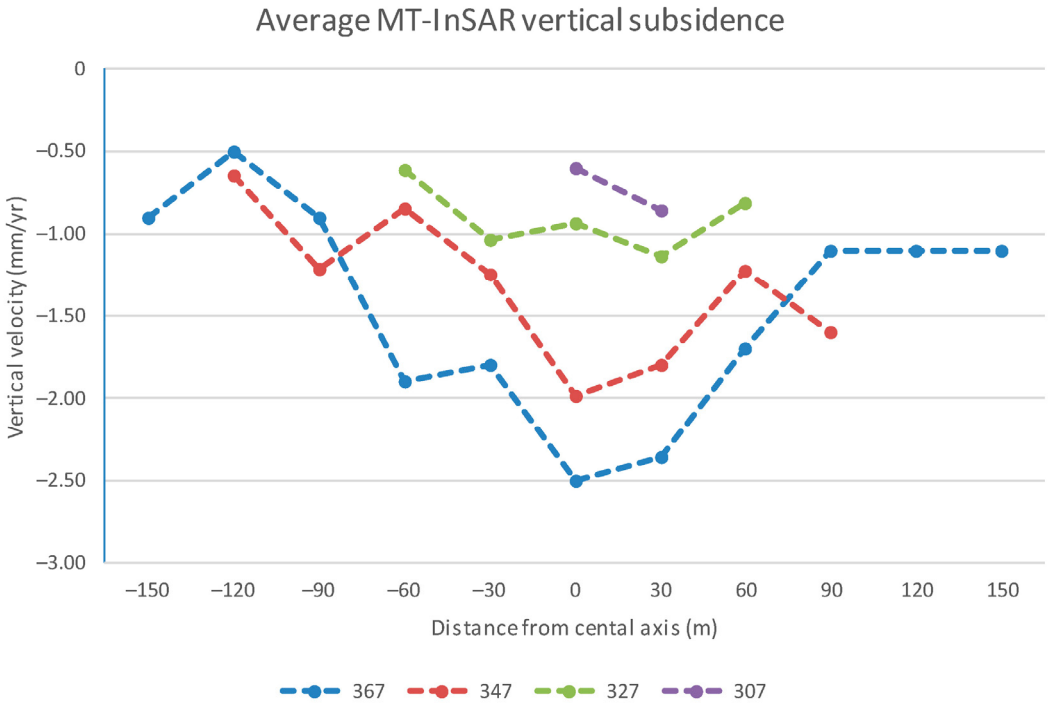

Figure 16. Evolution of dam vertical velocity (in mm/year) in Sentinel-1A/B period (2015–2021) in downstream slope of body dam in buffers of 10m around main points along berms (307, 327, 347) and crest of dam (367).

4.3. Measured Deformation: Topography and MT-InSAR

Topographical measurements were carried out unevenly at a low frequency (every 2–3 months in short 1–2-years periods covering the interval 2015–2018, with this period being the recorded deformation data currently available. MT-InSAR movements are available after each successful Sentinel-1 acquisition over the dam (with a revisit time of up to 6 days). The precision of the topography was around 25 mm (tolerance), whereas for MT-InSAR, it was around 1 mm/year (in velocity). For the analysis, the velocities measured via topography and MT-InSAR were compared for the overlap period (October 2015–August 2018), considering that the precision in velocities for MT-InSAR is higher than the topography.

Figure 17 shows the position of targets and gridded vertical velocity points for the period from September 2015 to August 2018.

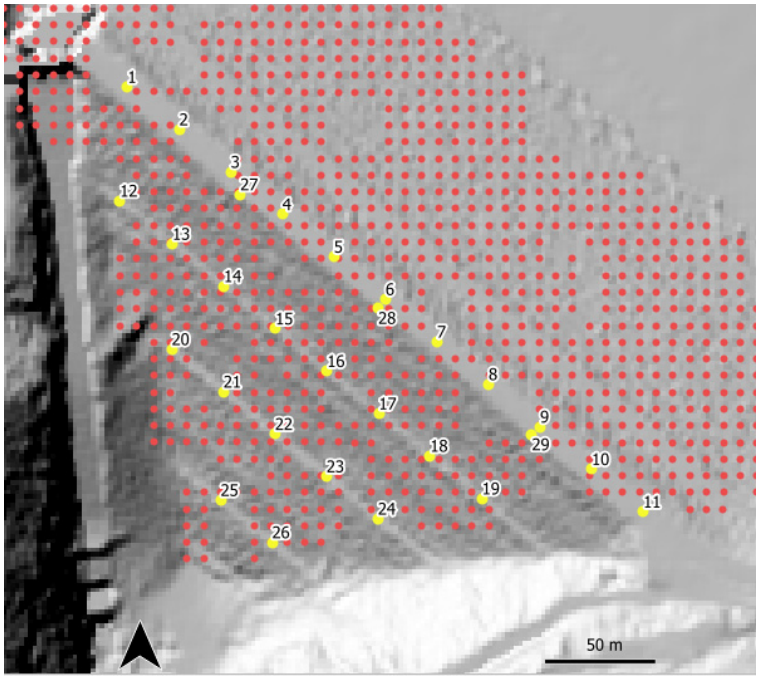

Figure 17. Position of topographic targets (yellow) and gridded vertical velocity points identified by Sentinel-1A/B MT-InSAR (red) on Benínar Dam.

In order to plot movements of targets and vertical velocity points, a previous analysis was performed. For each target point in the crest (numbered from 1 on the right bank to 11 in the left bank), a buffer of 10 m was selected through identifying the PS points in this range. Vertical measured velocities were plotted for each topographic target and compared to the average vertical velocity (mm/year) of points in the surrounding buffer (Figure 18).

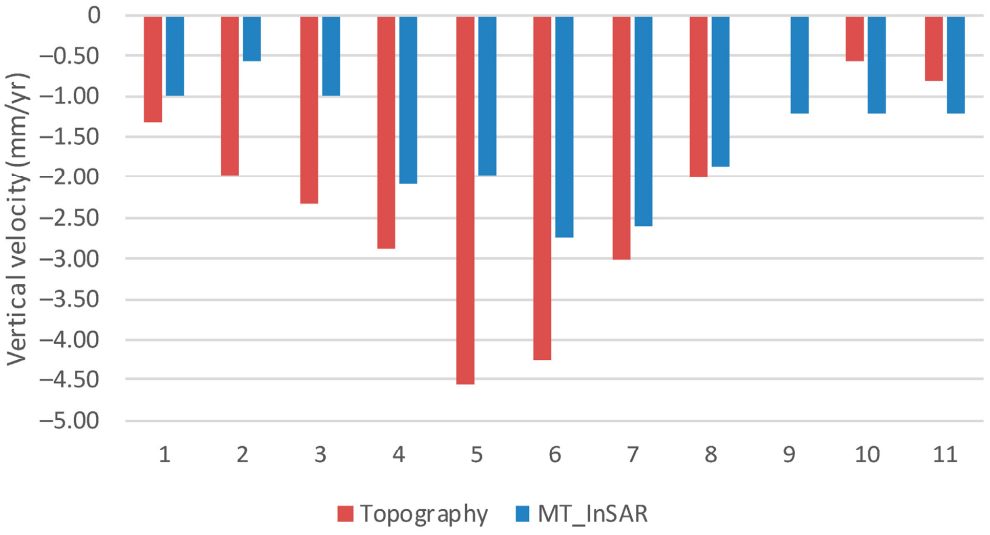

Figure 18. Benínar Dam crest plot for vertical velocity of displacements (mm/year) measured with topography (red) vs. average MT-InSAR vertical velocity for PS points (blue) in a 10 m buffer in overlap period from October 2015 to August 2018.

It can be noted that the magnitude of vertical displacements measured with topography is within the limit of instrumental tolerance. For this reason, auscultation reports consider that displacements are negligible, as they are less than the instrumental tolerance [42]. However, MT-InSAR analysis performed with Sentinel-1A/B data is sensitive to dam consolidation in the crest, showing the pattern in Figure 18 where maximum velocities

are reached around target 6, which is located in the center of the crest of the dam (the higher area over the foundations), with around −2.5 mm/year. This area shows a cumulated Z displacement of around −10 mm in the three monitored years, which is coherent with measured velocities. Targets 9 and 11 show excessive displacements in topography, which can be explained by the fact that they are measured from a distant reference point located in the opposite right bank, thus showing higher instrumental error.

4.4. Deformation Patterns in the Benínar Dam Area

MT-InSAR allows the monitoring of large areas in the dam and surroundings, as shown in Figure 19. The main dam, as well as the primary slopes that drain into the reservoir in both ascending and descending geometries, are densely covered by PS points.

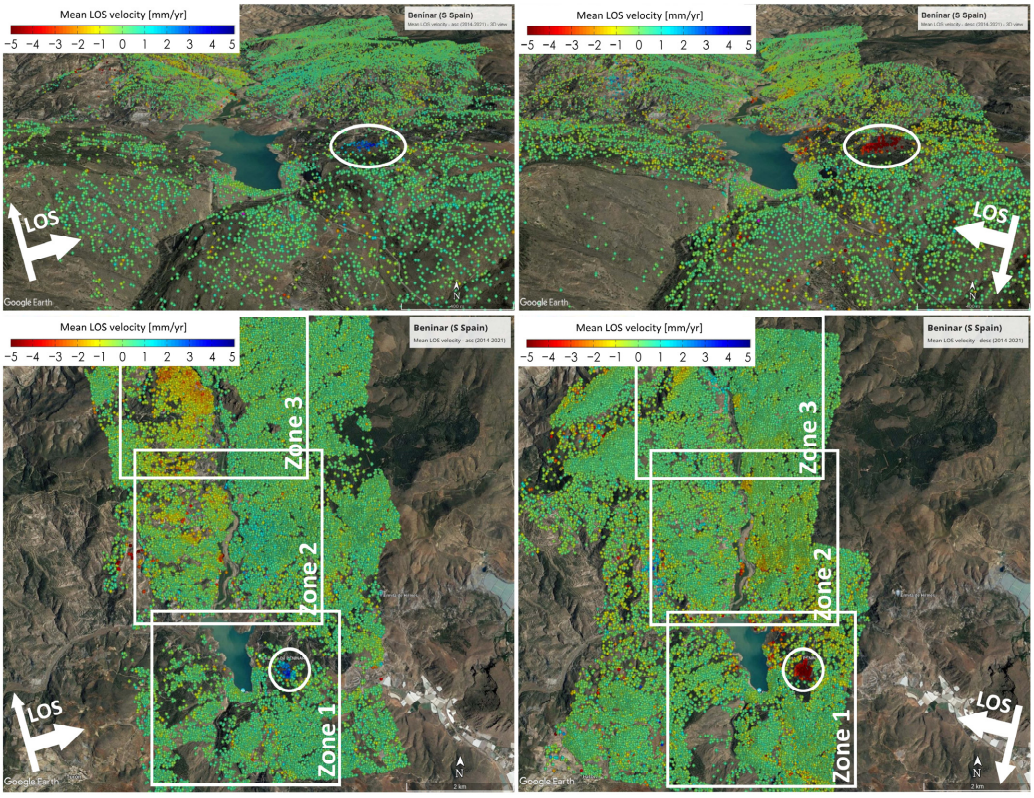

Figure 19. MT-InSAR monitoring of Benínar Dam: mean deformation velocity (mm/year) in line-of-sight (LOS) from Sentinel-1 ascending orbits (**left**) and descending orbits (**right**) between 2015 and 2021 (up: 3D view; low: plan view with zonation).

A detailed analysis of the monitored area shows the expected dam consolidation in Zone 1, with a local landslide located to the east of the dam (Figure 19). This landslide shows a classical pattern of PS that moves closer to the satellite in ascending orbit (blue points) while being further away from satellite in descending geometry, showing a combined downwards–westwards movement that is coherent with local topography. Zone 2 shows some small deformation in slopes located to the west of the valley. Finally, Zone 3 presents a large subsiding slope on the west side of the river and northwest from a village called Darrical. Figure 20 presents the decomposition of movements in vertical and East–West direction in Zone 1. It confirms the displacement of the landslide located to the northeast of the dam, exhibiting a subsiding and westwards movement. The decomposition indicates that this landslide has an accumulated vertical displacement of about –6 cm and an E–W movement of about –12 cm (movement to the West).

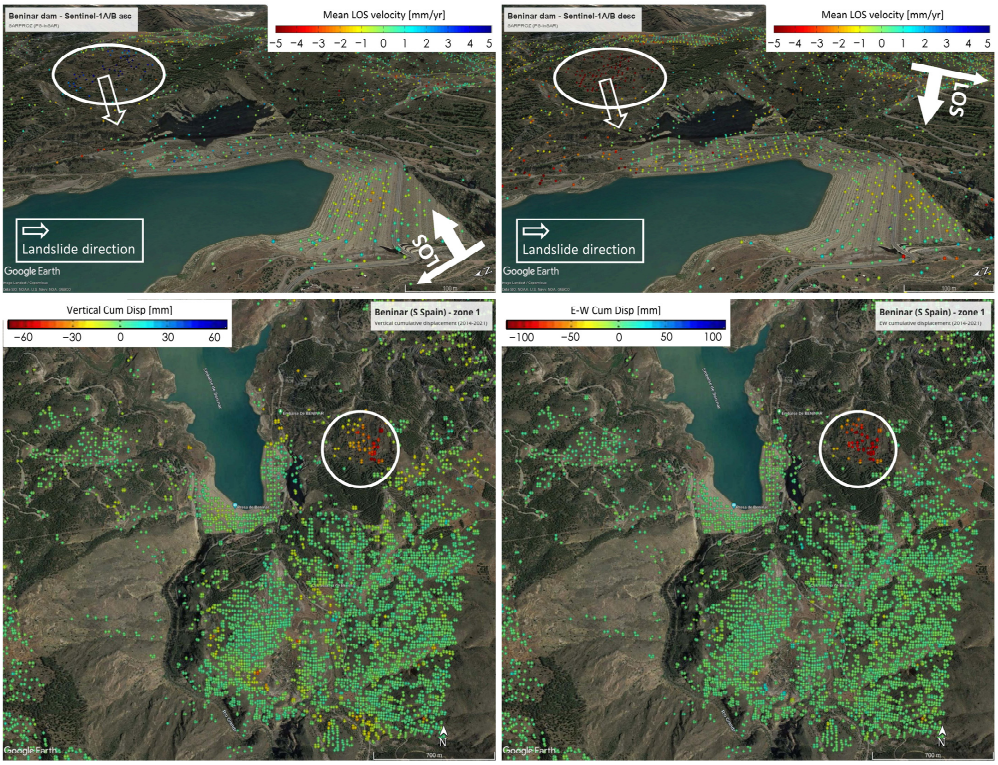

Figure 20. (**Top left**): Ascending Sentinel-1A/B LOS velocities. (**Top right**): Descending Sentinel-1A/B LOS velocities. (**Bottom left**): Cumulative displacements in vertical direction for period 2014–2021 in Dam area (zone 1). (**Bottom right**): Cumulative displacements in East–West direction for period 2014–2021 in Dam area (zone 1).

Figure 21 presents the decomposed vertical (left) and E–W (right) velocities. The motion of the large slope on the left (West slope) reveals a movement toward the channel with a vertical rate of subsidence (yellow–orange color) and net movement to the East (blue color). This large slope exhibits vertical movements of about −5 mm/year (downwards) and horizontal movements, toward the East, in the range 6–7 mm/year (Figure 21). This outcome can also be seen in the top image of Figure 22, where LOS velocities indicate the slide movement of the slopes. The bottom image of Figure 22 shows the slope in the background of Darrical village, where a landslide can be appreciated to the North of the village.

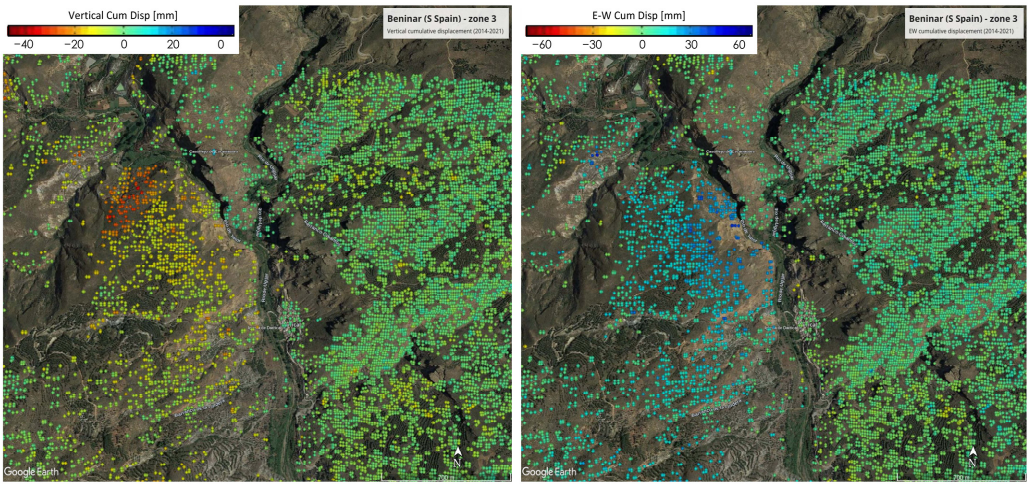

Figure 21. (**Left**): Cumulative displacements in vertical direction for period 2014–2021 in area of Darrical village (zone 3). (**Right**): Cumulative displacements in East–West direction for period 2014–2021 in area of Darrical village (zone 3).

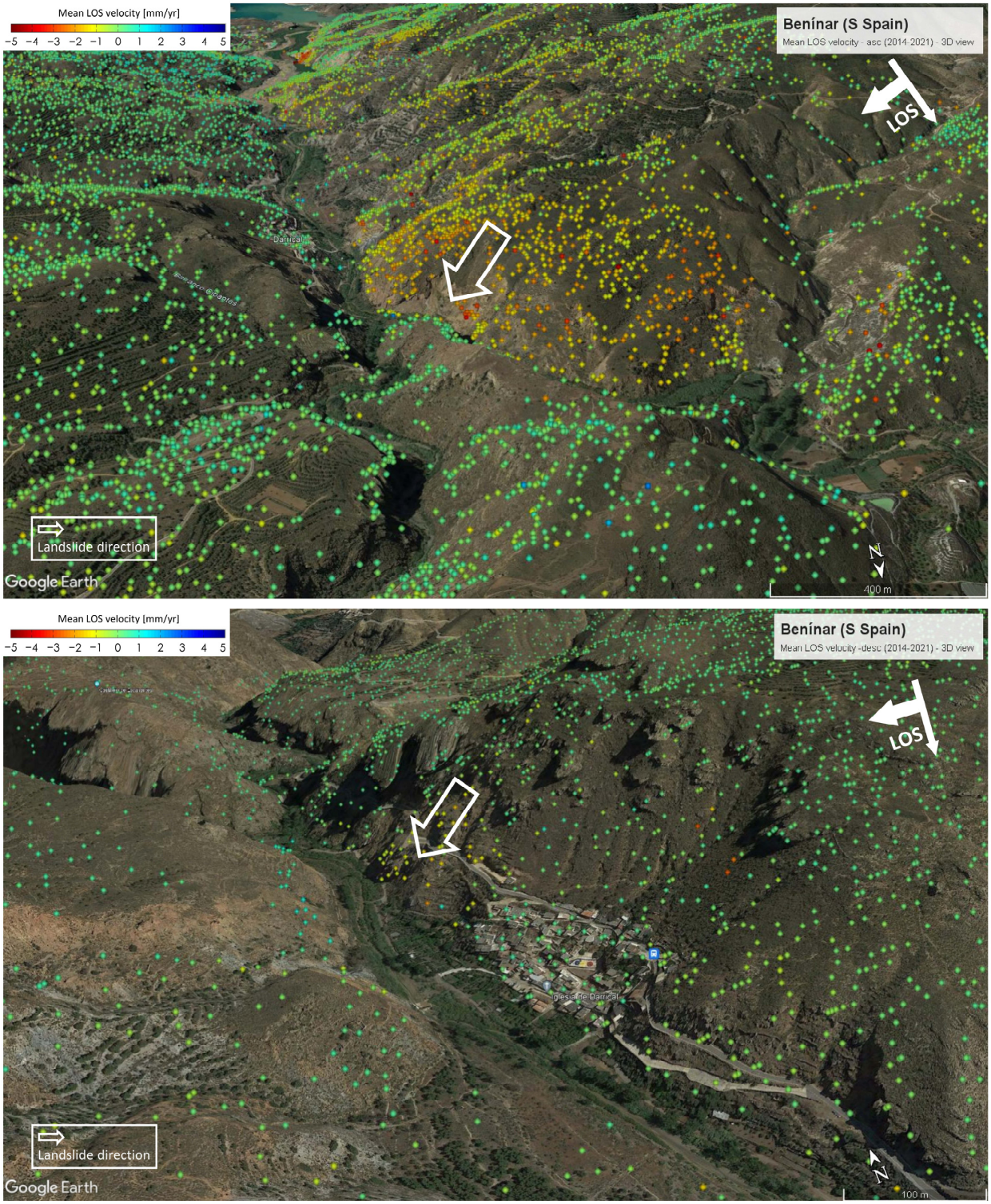

Figure 22. Landslides detected with Sentinel-1 Mean LOS velocity (mm/year). Top: in ascending pass, over western bank of river. Bottom: in descending pass to North of Darrical village.

5. Discussion

Upon completion of this research, a crucial issue that comes to light is the dependability of various monitoring technologies throughout the lifespan of a dam. Regarding the Benínar Dam, it is worth noting that most of the technologies installed were initially reported as non-operational since at least 2012 [28]. Moreover, the available data are sparse and unconnected, being reduced to topographical measurements from September 2015 to August 2018. In

contrast, MT-InSAR provided monthly deformation data from 1992, with small gaps between ERS and Envisat, and prior to the launch of Sentinel-1 constellation (Figure 23).

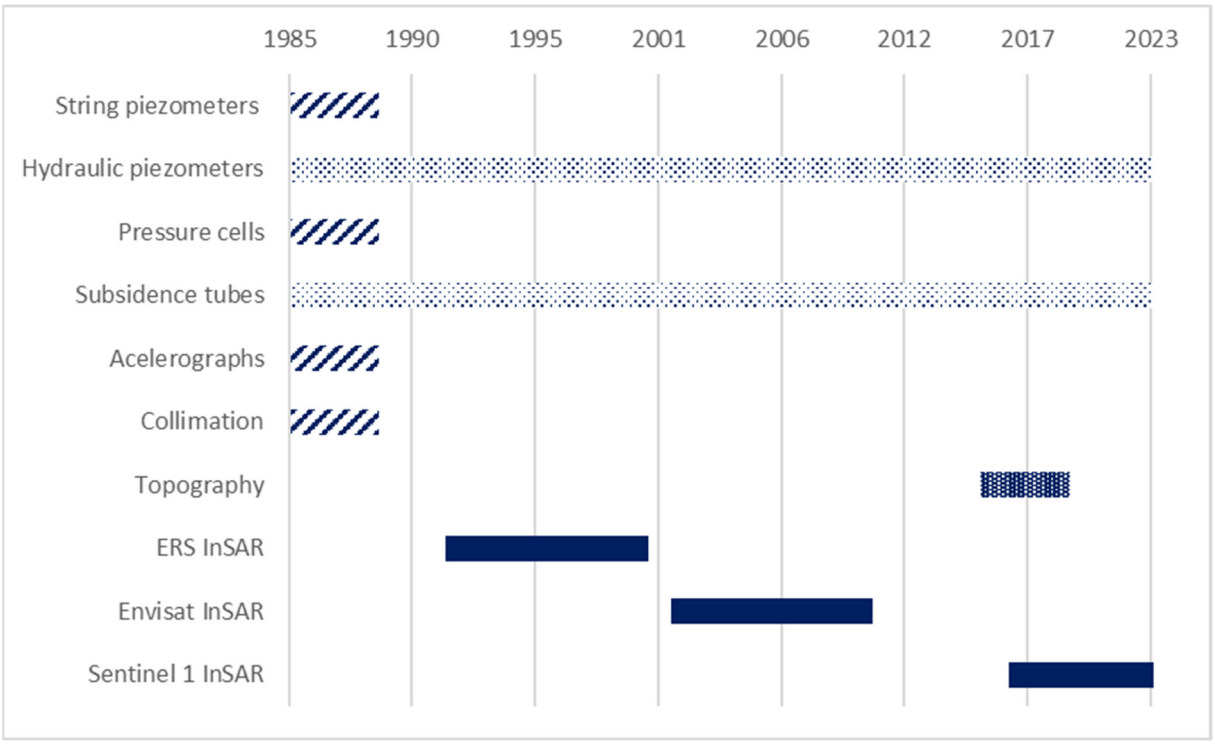

Figure 23. Evolution of monitoring systems at Benínar Dam (piezometers and subsidence tubes were expected to be operational, but no data were available).

Conventional topography at the Benínar Dam involved observing permanent targets directly during multiple campaigns without additional corrections, such as micro-geodesy. The resulting precision falls within the range of observed movements. Therefore, MT-InSAR is the most accurate technique available for analyzing the temporal deformation of this dam.

Integration of modeling is a key tool, as it allows predictions of the behavior of the dam in original design conditions, as opposed to the measured evolution. Stability, filtration, and deformation analyses were carried out at full reservoir, empty reservoir, and in a situation of rapid drawdown, enabling the estimation of the maximum movements admissible, i.e., around 19.25 cm in the crest axis, based on the section with the greatest movements occurring in the part closest to the upstream slope. The distribution of pore pressures in the areas of the filter, core, and transition contacts remains uniform with a general behavior compatible with stability, while no problems are observed in the fault area. This trend results in limit equilibrium for the minimum slip circle, indicating that the stability conditions are satisfied in all the hypotheses analyzed. The case with lower values corresponds to the hypothesis of total rapid drawdown. Similar results were obtained by Corsetti [52], who highlighted the potential of MT-InSAR long time series as a valuable calibration dataset in building reliable numerical models.

Concerning this type of dam, vertical movements are significantly more critical than horizontal movements, as evidenced by significant subsidence in higher sections over the foundations [53]. Classical topography methods allow us to obtain target points movements (X, Y, Z) for each campaign with relatively low precision compared to geotechnical instrumentation. The vertical displacements calculated with high-precision leveling are undoubtedly more accurate. Thus, leveling should be included in the topographic control of embankment dams as a complement to classical collimation.

Based on long temporal series and high-quality processing, MT-InSAR shows reliable results coherent with dam design and modeling. The observed deformation velocities are

consistent with the gradual consolidation of the Benínar Dam over time. The median values decreased from −2.6 and −3.0 mm/year during the initial monitoring periods (ERS-1990s and Envisat-2000s) to a vertical velocity of −1.3 mm/year during the Sentinel-1 A/B period from 2015 to 2021. In recent years, vertical and eastward movements were decomposed, with a main vertical component and negligible movements in the East–West direction. These findings align with other investigations on earth-fill dams constructed between 1980 and 2000, such as the Ataturk Dam, where the deformation velocity decreased from 8 mm/year during the 1990s to 5 mm/year between 2016 and 2020 [54]. The Mosul Dam also exhibited comparable deformation, with an average velocity of 6 mm/year between 2014 and 2019 [55].

MT-InSAR measured velocities, due to their statistical nature, are not affected by peaks and outlier measures, providing a close approximation to the real trend of the dam's behavior. Nevertheless, it constitutes an outstanding addition to a comprehensive monitoring system that ought to encompass the following constituents: (1) flow control through dam, (2) settlement tubes, (3) piezometers, and (4) long-term topographic control (preferably via 26evelling). Accurate 26evelling can adjust MT-InSAR measurements with low root mean square errors (RMSEs), achieving a difference of 2 mm/year [53].

One of the main advantages of MT-InSAR is its ability to monitor the dam and surrounding area at a low cost per unit of monitored land. These benefits are highlighted in other studies, as well as the main limitations, including vegetated areas, water or wetted areas, and sudden movements [56]. MT-InSAR was demonstrated to enable the control of landslides, slopes, auxiliary infrastructures, and the dam body with the same processing effort. This finding is particularly important since projected monitoring systems typically do not record with the same frequency and precision throughout the dam's lifetime.

The Integration of MT-InSAR deformation series and dam modelling is a challenge that requires the selection of a dam with SAR data from its construction, optimally in the Sentinel-1 period (2014-nowadays) through the integration of conventional auscultation with MT-InSAR. MT-InSAR series would record the deformation of the dam body and associate structures from its construction, including the main milestones, as the first full filling of the reservoir and, if possible, some drawdowns.

6. Conclusions

The outcomes of this research advocate for the combination of dam modeling and MT-InSAR monitoring of embankment dams throughout their lifecycles, including mature dams' ones, such as the Benínar Dam.

MT-InSAR was demonstrated to be a reliable and cost-effective system for monitoring deformations in embankment dams; however, it should be complemented with geodetic, hydraulic, and geotechnical monitoring, as required by dam safety regulations.

Temporal evolution of dam deformation was characterized spatially and temporally. Results are consistent with the theoretically modeled consolidation of the dam, indicating higher subsidence in the central parts of the dam, over the foundations, and in the initial recording period (1992–2000). Subsidence velocities decreased from maximum values of −6 mm/year in the 1992–2000 period to actual levels of −2 mm/year.

Dam modeling allows us to contrast the expected dam behavior and consolidation with the recorded measurements. In the case of the Benínar Dam, modeling confirms that the dam is stable both for full reservoir and a rapid drawdown.

Regarding topographic auscultation, trigonometric leveling showed uncertainties on the order of centimeters and was not sensitive enough to monitor dam consolidation after the initial fast settlement phase. The topographic records of many dams, such as the studied one, are not continuous and present "no-data" periods.

Long-term topographic control based on high-precision leveling should be conducted at low frequencies (1 or 2 per year) since MT-InSAR can provide accurate temporal resolution for the time between campaigns.

One of the main strengths of MT-InSAR for dam monitoring is the integration of the monitoring of the reservoir and associated infrastructures. This method provides high levels of temporal and spatial resolution in large areas at an affordable cost. MT-InSAR enabled a rapid identification and characterization of the main landslides and unstable areas in the reservoir and surrounding areas. The decomposition of ascending and descending geometries allowed for the determination of the main direction of several slow mass movements.

Future investigations should concentrate on establishing integrated monitoring systems with real-time interfaces to access data and receive notifications and warnings. Long-term monitoring series offer an excellent opportunity to build expert systems based on artificial intelligence to detect irregularities in the dam, infrastructures, and reservoir area.

Author Contributions: Conceptualization, M.M.-S., A.M.R.-A. and F.L.-F.; methodology, M.M.-S., A.M.R.-A., F.L.-F., B.G.-R., R.M.-M., D.P., J.M.D.-B. and M.B.; validation, M.M.-S., A.M.R.-A., F.L.-F., B.G.-R., R.M.-M., J.M.D.-B., M.L. and J.J.S.; formal analysis, M.M.-S., A.M.R.-A., F.L.-F., B.G.-R. and R.M.-M.; investigation, M.M.-S., A.M.R.-A., F.L.-F., B.G.-R., R.M.-M., J.M.D.-B., M.L., J.P. and J.J.S.; resources, M.M.-S., A.M.R.-A. and F.L.-F.; writing—original draft preparation, M.M.-S., A.M.R.-A., F.L.-F., B.G.-R. and R.M.-M. All authors have read and agreed to the published version of the manuscript.

Funding: Research was supported by the following projects: (a) ReMoDams project ESP2017-89344-R (AEI/FEDER, UE) from the Spanish Ministry of Economy, Industry and Competitiveness, (b) SIAGUA project PID2021-128123OB-C21 and PID2021-128123OB-C22 funded by (MCIN/AEI/10.13039/501100011033/FEDER,UE), (c) POAIUJA-2023/2024 and CEACTEMA from University of Jaén (Spain), and (d) the RNM-282 research group from the Junta de Andalucía (Spain).

Data Availability Statement: Not applicable.

Acknowledgments: ERS-1/2 and Envisat data sets were provided by the European Space Agency (ESA). Sentinel-1A/B data were freely provided by ESA through Copernicus Programme. Data were processed by DORIS (TUDelft), StaMPS (Andy Hooper), and SARPROZ (Copyright, 2009–2023, Daniele Perissin). The satellite orbits are from TUDelft and ESA, as well as from the ESA Quality Control Group of Sentinel-1. We thank Detektia Earth Surface Monitoring for their support in the visualization of topographic data and in using MT-InSAR. Authors acknowledge the Slovak APVV agency project APVV-19-0150. We acknowledge and thank the dam and validation data provided by the Dirección General de Infraestructuras del Agua (Consejería de Agricultura, Ganadería, Pesca y Desarrollo Sostenible de la Junta de Andalucía, Spain) and TYPSA.

Conflicts of Interest: The authors declare no conflict of interest.

References

1. ICOLD. World Register of Dams. *General Synthesis.* 2020. Available online: https://www.icold-cigb.org/ (accessed on 30 April 2020).
2. ICOLD. *Dam Failures-Statistical Analysis (Bulletin 99)*; Document protected by Copy Right; ICOLD: Paris, France, 1995.
3. Foster, M.; Fell, R.; Spannagle, M. The statistics of embankment dam failures and accidents. *Can. Geotech. J.* **2000**, *37*, 1000–1024. [CrossRef]
4. Estrela, T.; Pérez-Martin, M.A.; Vargas, E. Impacts of climate change on water resources in Spain. *Hydrol. Sci. J.* **2012**, *57*, 1154–1167. [CrossRef]
5. Forero-Ortiz, E.; Martínez-Gomariz, E.; Monjo, R. Climate Change Implications for Water Availability: A Case Study of Barcelona City. *Sustainability* **2020**, *12*, 1779. [CrossRef]
6. ICOLD. *Bulletin on Risk Assessment in Dam Safety Management*; International Commission on Large Dams: Paris, France, 2003.
7. Fluixá-Sanmartín, J.; Altarejos-García, L.; Morales-Torres, A.; Escuder-Bueno, I. Climate change impacts on dam safety. *Nat. Hazards Earth Syst. Sci.* **2018**, *18*, 2471–2488. [CrossRef]
8. Bowles, D.; Brown, A.; Hughes, A.; Morris, M.; Sayers, P.; Topple, A.; Wallis, M.; Gardiner, K. *Guide to Risk Assessment for Reservoir Safety Management, Volume 1: Guide*; Environment Agency: Bristol, UK, 2013.
9. USBR. *Climate Change Adaptation Strategy: 2016 Progress Report*; U.S. Department of the Interior, Bureau of Reclamation: Washington, DC, USA, 2016.
10. USACE. *Guidance for Incorporating Climate Change Impacts to Inland Hydrology in Civil Works Studies, Designs, and Projects (Engineering and Construction Bulletin (ECB 2016-25)*; USACE: Washington, DC, USA, 2016.
11. Gabriel, A.K.; Goldstein, R.M.; Zebker, H.A. Mapping small elevation changes over large areas: Differential radar interferometry. *J. Geophys. Res.* **1989**, *94*, 9183–9191. [CrossRef]
12. Bamler, R.; Hartl, P. Synthetic aperture radar interferometry. *Inverse Probl.* **1998**, *14*, R1-54. [CrossRef]

13. Rosen, P.A.; Hensley, S.; Joughin, I.R.; Li, F.K.; Madsen, S.N.; Rodriguez, E.; Goldstein, R.M. Synthetic Aperture Radar Interferometry. *Proc. IEEE* **2000**, *88*, 333–382. [CrossRef]
14. Ferretti, A.; Prati, C.; Rocca, F. Permanent scatterers in SAR interferometry. *IEEE Trans. Geosci. Remote Sens.* **2001**, *39*, 8–20. [CrossRef]
15. Hooper, A.; Zebker, H.; Segall, P.; Kampes, B. A new method for measuring deformation on volcanoes and other natural terrains using InSAR persistent scatterers. *Geophys. Res. Lett.* **2004**, *31*, L23611. [CrossRef]
16. Kampes, B.M. *Radar Interferometry: Persistent Scatterer Technique, Radar Interferometry: Persistent Scatterer Technique*; Springer: Dordrecht, The Netherlands, 2006. [CrossRef]
17. Berardino, P.; Fornaro, G.; Lanari, R.; Sansosti, E. A new algorithm for surface deformation monitoring based on small baseline differential SAR interferograms. *IEEE Trans. Geosci. Remote Sens.* **2002**, *40*, 2375–2383. [CrossRef]
18. Schmidt, D.A.; Bürgmann, R. Time-dependent land uplift and subsidence in the Santa Clara valley, California, from a large interferometric synthetic aperture radar data set. *J. Geophys. Res. Solid Earth* **2003**, *108*, 2416. [CrossRef]
19. Hooper, A. A multi-temporal InSAR method incorporating both persistent scatterer and small baseline approaches. *Geophys. Res. Lett.* **2008**, *35*, L16302. [CrossRef]
20. Hooper, A.; Bekaert, D.; Spaans, K.; Arikan, M. Recent advances in SAR interferometry time series analysis for measuring crustal deformation. *Tectonophysics* **2012**, *514*, 1–13. [CrossRef]
21. Zhu, M.; Wan, X.; Fei, B.; Qiao, Z.; Ge, C.; Minati, F.; Vecchioli, F.; Li, J.; Costantini, M. Detection of Building and Infrastructure Instabilities by Automatic Spatiotemporal Analysis of Satellite SAR Interferometry Measurements. *Remote Sens.* **2018**, *10*, 1816. [CrossRef]
22. Susaki, J.; Maruo, N.; Tsujino, M.; Boonyatee, T. Detection of differential settlement of man-made structures coupled with urban development by using persistent scatterer interferometry (PSI). *Remote Sens.* **2018**, *10*, 1048. [CrossRef]
23. García, A.J.; Marchamalo, M.; Martínez, R.; González-Rodrigo, B.; González, C. Integrating Geotechnical and SAR Data for the Monitoring of Underground Works in the Madrid Urban Area: Application of the Persistent Scatterer Interferometry Technique. *Int. J. Appl. Earth Obs. Geoinf.* **2019**, *74*, 27–36. [CrossRef]
24. Tomás, R.; Cano, M.; García-Barba, J.; Vicente, F.; Herrera, G.; Lopez-Sanchez, J.M.; Mallorquí, J.J. Monitoring an earthfill dam using differential SAR interferometry: La Pedrera dam, Alicante, Spain. *Eng. Geol.* **2013**, *157*, 21–32. [CrossRef]
25. Ruiz-Armenteros, A.M.; Lazecky, M.; Hlaváčová, I.; Bakoň, M.; Delgado, J.M.; Sousa, J.J.; Lamas-Fernández, F.; Marchamalo, M.; Caro-Cuenca, M.; Papco, J.; et al. Deformation monitoring of dam infrastructures via spaceborne MT-InSAR. The case of La Viñuela (Málaga, southern Spain). *Procedia Comput. Sci.* **2018**, *138*, 346–353. [CrossRef]
26. Al-Husseinawi, Y.; Li, Z.; Clarke, P.; Edwards, S. Evaluation of the Stability of the Darbandikhan Dam after the 12 November 2017 Mw 7.3 Sarpol-e Zahab (Iran–Iraq Border) Earthquake. *Remote Sens.* **2018**, *10*, 1426. [CrossRef]
27. El-Askary, H.; Fawzy, A.; Thomas, R.; Li, W.; LaHaye, N.; Linstead, E.; Piechota, T.; Struppa, D.; Sayed, M.A. Assessing the Vertical Displacement of the Grand Ethiopian Renaissance Dam during Its Filling Using DInSAR Technology and Its Potential Acute Consequences on the Downstream Countries. *Remote Sens.* **2021**, *13*, 4287. [CrossRef]
28. THIGSA. *Estudio e Investigación de los Procesos de Filtración y Fenómenos Geológicos Anómalos en la Presa de Beninar*; Técnicas de Investigación Hidrogeológica: Sevilla, Spain, 2012.
29. CEDEX. *Estudio Hidrodinámico de Detalle de la Cuenca de Recepción del Embalse de Benínar*; Centro de Experimentación para las Obras Públicas: Madrid, Spain, 1990.
30. MITECO. Automatic Hydrological Information System (S.A.I.H.). 2022. Available online: https://www.miteco.gob.es (accessed on 30 November 2022).
31. Diaz de Federico, A.; Puga, E. Estudio Geológico del Complejo Sierra Nevada Hacia el Manto Alcázar. *Tecniterrae* **1976**, *9*, 26–35.
32. IGME. Cartografía Geológica Digital Continua a Escala 1:50.000. *GEODE. Servicio WMS GEODE. © NC Instituto Geológico y Minero de España (IGME).* 2004. Available online: http://mapas.igme.es/gis/services/Cartografia_Geologica/IGME_Geode_50/MapServer/WMSServer (accessed on 30 November 2022).
33. IGME. Mapa Geológico de España a Escala 1:50.000. *Segunda Serie (MAGNA). Hoja Berja (© NC Instituto Geológico y Minero de España (IGME).* 1977. Available online: http://info.igme.es (accessed on 30 November 2022).
34. Adamo, N.; Sissakian, V.K.; Al-Ansari, N.; Elagely, M.; Knutsson, S.; Laue, J. Dam Safety Problems Related to Seepage. *J. Earth Sci. Geotech. Eng.* **2020**, *10*, 1792–9660.
35. MITMA. Ministerio de Transportes, Movilidad y Agenda Urbana. 2022. Available online: https://www.mitma.gob.es/organos-colegiados/comision-permanente-de-normas-sismorresistentes/cpns/normativa (accessed on 5 July 2022).
36. Cremer, C.; Pecker, A.; Davenne, L. Modelling of nonlinear dynamic behavior of a shallow strip foundation with macro-element. *J. Earthq. Eng.* **2002**, *6*, 175–211. [CrossRef]
37. Alonso Pérez de Agreda, E. *Estabilidad de Taludes. Enginyeria del Terreny, Cartogràfica i Geofísica*; ETS Ingeniería de Caminos Canales y Puertos, Universidad Politécnica de Cataluña: Barcelona, Spain, 2005; Available online: https://deca.upc.edu/ca/el-departament/seccions/etcg (accessed on 30 November 2022).
38. Sanhueza Plaza, C.; Rodríguez Cifuentes, L. Comparative analysis of slope stability methods applied to natural slopes. *Rev. Constr.* **2013**, *12*, 17–29. [CrossRef]
39. SPANCOLD. *Guía Técnica de Seguridad de Presas Nº 2: "Criterios para Proyectos de Presas y sus Obras Anejas"*; Comité Español de Grandes Presas, Ministerio de Fomento, Gobierno de España: Madrid, Spain, 2012.

40. Ministerio de Fomento. Norma de Construcción Sismorresistente: Parte General y Edificación. In *NCSE-02*; Ministerio de Fomento, Servicio Virtual de Publicaciones; Gobierno de España: Madrid, Spain, 2009.
41. Duncan, J.M.; Brandon, T.L.; Wright, S.G.; Vroman, N. Stability of I-Walls in New Orleans during Hurricane Katrina. *J. Geotech. Geoenvironmental Eng.* **2008**, *134*, 681–691. [CrossRef]
42. AIMA Ingeniería. *Sistema de Auscultación Topográfica de la Presa de Benínar. Distrito Hidrográfico del Mediterráneo. Provincia de Almería. Junta de Andalucía. Agencia de Medio Ambiente y Agua. Expediente NET 042467/1. Informes de 2015 a 2018*; AIMA Ingeniería: El Ejido, Spain, 2018.
43. Ferretti, A.; Prati, C.; Rocca, F. Nonlinear subsidence rate estimation using permanent scatterers in differential SAR interferometry. *IEEE Trans. Geosci. Remote Sens.* **2000**, *38*, 2202–2212. [CrossRef]
44. Ketelaar, V.B.H. *Técnicas de Monitorização da Subsidência de Interferometria por Radar de Satélite*; Springer: Dordrecht, The Netherlands, 2009. [CrossRef]
45. Bakon, M.; Perissin, D.; Lazecky, M.; Papco, J. Infrastructure Non-linear Deformation Monitoring via Satellite Radar Interferometry. *Procedia Technol.* **2014**, *16*, 294–300. [CrossRef]
46. Hooper, A.; Bekaert, D.; Spaans, K. *StaMPS/MTI Manual, version 3.3b1*; School of Earth and Environment, University of Leeds: Leeds, UK, 2013; Available online: https://homepages.see.leeds.ac.uk/~earahoo/stamps/StaMPS_Manual_v3.3b1.pdf (accessed on 30 November 2022).
47. Perissin, D.; Wang, T. Repeat-pass SAR interferometry with partially coherent targets. *IEEE Trans. Geosci. Remote Sens.* **2011**, *50*, 271–280. [CrossRef]
48. Perissin, D. SARPROZ Software. Official Product Web Page. 2023. Available online: http://www.sarproz.com (accessed on 15 March 2023).
49. ASF; DAAC. Alaska State Facility (ASF) Distributed Active Archive Centre (DAAC). Official Web Page. 2020. Available online: https://asf.alaska.edu (accessed on 24 March 2023).
50. Lei, L.; Perissin, D.; Qin, Y. Change Detection with Spaceborne InSAR Techniques in Hong Kong. In Proceedings of the 2013 IEEE International Geoscience and Remote Sensing Symposium—IGARSS, Melbourne, Australia, 21–26 July 2013.
51. SPANCOLD. *Seguridad de Presas P-1, Guías Técnicas de Seguridad de Presas*; Comité Nacional Español de Grandes Presas: Madrid, Spain, 2005; ISBN 84-89567-15-8.
52. Corsetti, M.; Fossati, F.; Manunta, M.; Marsella, M. Advanced SBAS-DInSAR Technique for Controlling Large Civil Infrastructures: An Application to the Genzano di Lucania Dam. *Sensors* **2018**, *18*, 2371. [CrossRef] [PubMed]
53. Wang, Q.Q.; Huang, Q.H.; He, N.; He, B.; Wang, Z.C.; Wang, Y.A. Displacement monitoring of upper Atbara dam based on time series InSAR. *Surv. Rev.* **2020**, *52*, 485–496. [CrossRef]
54. Bayik, C.; Abdikan, S.; Arıkan, M. Long term displacement observation of the Atatürk Dam, Turkey by multi-temporal InSAR analysis. *Acta Astronaut.* **2021**, *189*, 483–491. [CrossRef]
55. Othman, A.A.; Al-Maamar, A.F.; Al-Manmi, D.A.M.; Liesenberg, V.; Hasan, S.E.; Al-Saady, Y.I.; Shihab, A.T.; Khwedim, K. Application of DInSAR-PSI technology for deformation monitoring of the Mosul Dam, Iraq. *Remote Sens.* **2019**, *11*, 2632. [CrossRef]
56. Grebby, S.; Sowter, A.; Gluyas, J.; Toll, D.; Gee, D.; Athab, A.; Girindran, R. Advanced analysis of satellite data reveals ground deformation precursors to the Brumadinho Tailings Dam collapse. *Commun. Earth Environ.* **2021**, *2*, 2. [CrossRef]